Available online at www.sciencedirect.com

ScienceDirect

Geochimica et Cosmochimica Acta 221 (2018) 379–405

Geochimica et Cosmochimica Acta

www.elsevier.com/locate/gca

Presolar silicates in the matrix and fine-grained rims around chondrules in primitive CO3.0 chondrites: Evidence for pre-accretionary aqueous alteration of the rims in the solar nebula

Pierre Haenecour [a,b,c,d,*], Christine Floss [a,c], Thomas J. Zega [d,e], Thomas K. Croat [a,c], Alian Wang [b,c], Bradley L. Jolliff [b,c], Paul Carpenter [b,c]

[a] *Laboratory for Space Sciences and Physics Department, Washington University in St. Louis, One Brookings Drive, St. Louis, MO 63130-4899, USA*

[b] *Department of Earth and Planetary Sciences, Washington University in St. Louis, One Brookings Drive, St. Louis, MO 63130-4899, USA*

[c] *McDonnell Center for the Space Sciences, Washington University in St. Louis, One Brookings Drive, St. Louis, MO 63130-4899, USA*

[d] *Lunar and Planetary Laboratory, The University of Arizona, 1629 E. University Blvd., Kuiper, Space Science Bldg, Tucson, AZ 85721-0092, USA*

[e] *Department of Material Science and Engineering, The University of Arizona, 1235 E. James E. Rogers Way, Tucson, AZ 85721-0012, USA*

Received 1 October 2016; accepted in revised form 1 June 2017; available online 8 June 2017

Abstract

To investigate the origin of fine-grained rims around chondrules (FGRs), we compared presolar grain abundances, elemental compositions and mineralogies in fine-grained interstitial matrix material and individual FGRs in the primitive CO3.0 chondrites Allan Hills A77307, LaPaz Icefield 031117 and Dominion Range 08006. The observation of similar overall O-anomalous (~155 ppm) and C-anomalous grain abundances (~40 ppm) in all three CO3.0 chondrites suggests that they all accreted from a nebular reservoir with similar presolar grain abundances. The presence of presolar silicate grains in FGRs combined with the observation of similar estimated porosity between interstitial matrix regions and FGRs in LAP 031117 and ALHA77307, as well as the identification of a composite FGR (a small rimmed chondrule within a larger chondrule rim) in ALHA77307, all provide evidence for a formation of FGRs by accretion of dust grains onto freely-floating chondrules in the solar nebula before their aggregation into their parent body asteroids. Our study also shows systematically lower abundances of presolar silicate grains in the FGRs than in the matrix regions of CO3 chondrites, while the abundances of SiC grains are the same in all areas, within errors. This trend differs from CR2 chondrites in which the presolar silicate abundances are higher in the FGRs than in the matrix, but similar to each other within 2σ errors. This observation combined with the identification of localized (micrometer-scaled) aqueous alteration in a FGR of LAP 031117 suggests that the lower abundance of presolar silicates in FGRs reflects pre-accretionary aqueous alteration of the fine-grained material in the FGRs. This pre-accretionary alteration could be due to either hydration and heating of freely floating rimmed chondrules in icy regions of the solar nebula

* Corresponding author at: The University of Arizona, 1629 E. University Blvd., Kuiper Space Science Bldg., Tucson, AZ 85721-0092, USA.

E-mail address: pierre@lpl.arizona.edu (P. Haenecour).

http://dx.doi.org/10.1016/j.gca.2017.06.004

0016-7037/© 2017 Elsevier Ltd. All rights reserved.

or melted water ice associated with ^{26}Al-related heating inside precursor planetesimals, followed by aggregation of FGRs into the CO chondrite parent-body.
© 2017 Elsevier Ltd. All rights reserved.

Keywords: Carbonaceous chondrites; Circumstellar grains; Early solar system history; Fine-grained chondrule rims; NanoSIMS; Nebular processes; Pre-accretionary alteration; Presolar grains; Stardust; Solar Nebula

1. INTRODUCTION

Like sedimentary conglomerates, primitive carbonaceous chondrites are physical aggregates of sub-millimeter to millimeter-sized coarse-grained components such as chondrules, calcium–aluminum-rich inclusions (CAIs), amoeboid olivine aggregates (AOAs) and Fe-Ni metal grains, consolidated in a matrix of fine-grained material (e.g., Buseck and Hua, 1993; Scott and Krot, 2014). They are among the oldest and most primitive rocks in the Solar System and, thus, constitute essential objects to study the processes that operated during the formation and early evolution of the Solar System. In addition to its presence as interstitial matrix, fine-grained material in meteorites also occurs as rims around chondrules and CAIs, and corresponds to the optically opaque (in thin section) complex mixture of small (<5 μm) crystalline and amorphous grains (e.g., silicates, oxides, sulfides, Fe-Ni metallic and carbonates) and carbonaceous matter in chondrites (e.g., McSween and Huss, 2010; Scott and Krot, 2014). The fine-grained materials in some chondrites (often the least altered) also contain tiny (nanometer- to micrometer-size) presolar grains, which formed in circumstellar environments and stellar ejecta (e.g., Zinner, 2014; Floss and Haenecour, 2016a).

Although fine-grained materials and their relationships to chondrules have been investigated for decades, their origin(s) remain unclear (e.g., McSween and Huss, 2010; Scott and Krot, 2014). In particular, the origin of fined-grained chondrule rims (FGRs) in many carbonaceous chondrites and the possible relationship of these rims to chondrules and/or matrix materials is still uncertain.

Through the years, several models for the formation of fine-grained chondrule rims (FGRs) have been proposed, including direct formation of the rims from adjacent chondrule material (e.g., re-condensation of chondrule volatile elements or disaggregated chondrule material; e.g., Sears, 2011), formation by dust accretion onto freely floating chondrules in the solar nebula before the incorporation of the chondrules into planetesimals (e.g., Allen et al., 1980; King and King, 1981; Wilkening and Hill, 1985; Metzler et al., 1992; Brearley, 1993; Morfill et al., 1998; Ciesla et al., 2003; Vogel et al., 2003; Zega and Buseck, 2003; Cuzzi, 2004; Metzler, 2004; Greshake et al., 2005; Ormel et al., 2008), or formation by the impact-related compression of fine-grained matrix material around chondrules on the meteorite parent-bodies (e.g., Sears et al., 1993; Tomeoka and Tanimura, 2000; Trigo-Rodriguez et al., 2006; Takayama and Tomeoka, 2012; Wasson and Rubin, 2014). Recently, Bland et al. (2011) suggested an intermediate model in which FGRs formed in two steps with initial accretion of the rims around freely floating chondrules in the solar nebula, followed by compression of the rims via numerous low-intensity shocks or low-pressure impacts between rimmed chondrules before accretion onto a parent body.

Presolar materials include a variety of high-temperature minerals and amorphous assemblages (from a few nanometers to several micrometers in diameter) such as nanodiamonds, silicon carbide (SiC), graphite, titanium carbide, oxides (e.g., corundum, spinel, hibonite, magnesiowüstite), silicon nitride, and silicates (e.g., olivine, pyroxene, silica) (e.g., Bernatowicz et al., 1987; Lewis et al., 1987; Amari et al., 1990; Zinner, 2014; Floss and Haenecour, 2016a). The laboratory study of presolar grains has traditionally been focused on obtaining information about stellar and interstellar grain formation, stellar evolution, physical properties in stellar environments, nucleosynthesis processes, and galactic chemical evolution (e.g., Zinner, 2014). However, by comparing the abundances of carbon-rich presolar grains (SiC, graphites and diamond) in different groups of primitive chondritic meteorites, studies (Huss and Lewis, 1994, 1995; Huss et al., 1997, 2003) have also suggested that presolar grains can constitute sensitive monitors of nebular and parent body processing in chondritic materials.

Because presolar silicates are more susceptible to heating and secondary processing than other, more refractory, presolar phases (e.g., SiC; Floss and Stadermann, 2012), they can provide new constraints on the accretion and compaction history of primitive meteorites. The discovery and characterization of presolar silicate grains in IDPs (Messenger et al., 2003, 2005), primitive carbonaceous chondrites (Floss and Stadermann, 2009a; Bose et al., 2012; Leitner et al., 2012; Nguyen and Zinner, 2004; Vollmer et al., 2009b; Nguyen et al., 2010) and Antarctic micrometeorites (Yada et al., 2008; Haenecour et al., 2012) has confirmed this suggestion. Indeed, comparison of presolar silicate abundances, the elemental compositions of presolar silicates (e.g. Fe contents) and the silicate/oxide ratios in various extraterrestrial materials can provide information about the influence of secondary processing, such as aqueous and thermal alteration, in primitive chondrites, as well as about the possible terrestrial alteration of meteoritic materials (Floss and Stadermann, 2012; Leitner et al., 2012; Floss and Haenecour, 2016a).

The petrographic classifications of ordinary and carbonaceous chondrites correlate with the degrees of aqueous alteration and/or metamorphism that they experienced on their parent-body asteroids (Krot et al., 2014). In particular, Ornans-type carbonaceous chondrites (CO) are characterized by a coherent group of petrologic type-3 chondrites

with a metamorphic sequence from type 3.0 (the most pristine) to 3.8 (nearly equilibrated; e.g., McSween, 1977; Scott and Jones, 1990; Sears et al., 1991). According to the Meteorite Bulletin Database (May 30, 2017), there are 556 meteorites classified as CO chondrites but only a few of these (< 20) have been classified as pristine type 3.0, including the Antarctic samples Allan Hills A77307 (ALHA77307), LaPaz Icefield 031117 (LAP 031117) and Dominion Range 08006 (DOM 08006). Based on the mean chromium content in ferroan chondrule olivine (Grossman and Brearley, 2005; Chizmadia and Cabret-Lebron, 2009; Davidson et al., 2014b) and Raman measurements (Bonal et al., 2007, 2016), these three meteorites have been classified as CO3.0 chondrites.

To explore the role of nebular and/or parent-body processing in the accretion and compaction of fine-grained material in primitive meteorites, we searched for presolar grains in the matrix and several FGRs from the CO3.0 carbonaceous chondrites LAP 031117, ALHA77307 and DOM 08006. Because these meteorites are thought to have experienced only minimal parent-body processing, they can provide direct information on other processes affecting fine-grained material in early solar system history. Here we report the first self-consistent data set of presolar grain abundances for discrete matrix regions and individual FGRs in three CO3.0 chondrites and use these data to discuss possible models of fine-grained rim formation around chondrules. Most studies of FGRs are based on meteorites that have experienced significantly more extensive secondary processing (e.g., Metzler et al., 1992; Lauretta et al., 2000; Tomeoka and Tanimura, 2000; Zega and Buseck, 2003; Trigo-Rodriguez et al., 2006; Takayama and Tomeoka, 2012; Leitner et al., 2016b) than the three meteorites in this study. However, the meteorites in our study are among the most primitive CO3 chondrites and, thus, provide more direct information on the earliest processes responsible for the formation of FGRs. Preliminary results were reported in Haenecour and Floss (2011, 2012), Haenecour et al. (2013a, 2014, 2015, 2017).

2. SAMPLES AND EXPERIMENTAL METHODS

2.1. Meteorite samples: CO3.0 chondrites

Polished thin-sections of the CO3 carbonaceous chondrites LAP 031117, ALHA77307 and DOM 08006 were obtained from the meteorite curatorial facility at NASA Johnson Space Center, Houston TX, USA (Fig. 1). Like type-3 ordinary chondrites, CO carbonaceous chondrites are classified into a metamorphic sequence from type 3.0 (e.g. ALHA77307) to 3.8 (e.g., Isna) based on the correlation between the mean chromium (Cr) content in ferroan olivine of type II chondrules and the distribution of Cr contents (Chizmadia et al., 2002; Grossman and Brearley, 2005; Davidson et al., 2014b). Note that, in this study, we use the terms 'pristine' and 'primitive' interchangeably to refer to the lack of evidence for pre-terrestrial thermal metamorphism and aqueous alteration.

ALHA77307 is highly unequilibrated and contains a high abundance of opaque, fine-grained matrix largely composed of amorphous silicate material with small amounts of magnesium-rich olivine, low-calcium pyroxene, Fe-Ni metal (e.g. kamacite), magnetite, and sulfides (Brearley, 1993). Grossman and Brearley (2005) showed that ferroan chondrule olivines in ALHA77307 have a mean Cr_2O_3 content of 0.38 ± 0.07 wt.%, suggesting that it is one of the most pristine CO chondrite (type 3.0). Except for the local occurrence of some phyllosilicate phases within amorphous matrix material and veins of anhydrite, Brearley (1993) showed that the matrix of ALHA77307 is essentially anhydrous and does not exhibit any other signs of thermal or aqueous alteration. This study also noted that the elemental compositions and mineralogies of matrix areas and fine-grained rims in ALHA77307 are very similar.

Chizmadia and Cabret-Lebron (2009) compared the fayalite contents in olivines from amoeboid olivine inclusions (AOIs, mean Fa content $= 0.56 \pm 0.21$ wt.%) and the mean Cr_2O_3 content in FeO-rich olivine chondrules (mean $Cr_2O_3 = 0.39 \pm 0.12$ wt.%) in LAP 031117 with other CO3 chondrites from Grossman and Brearley (2005), and showed that both parameters in LAP 031117 are more similar to those observed in ALHA77307. Apart from the presence of sporadic terrestrial alteration (Fe-rich) veins, Chizmadia and Cabret-Lebron (2009) did not identify any evidence of thermal metamorphism or aqueous alteration, and type I porphyritic chondrules and AOAs do not show any sign of Fe enrichment or incipient veining as commonly found in CO3 chondrites of higher petrologic subtypes (>CO3.1). All these observations led Chizmadia and Cabret-Lebron (2009) to classify LAP 031117 as a type 3.0 CO chondrite.

More recent studies (Davidson et al., 2014b; Simon and Grossman, 2015) have reported the identification of a new CO3.0 chondrite, DOM 08006, which exhibits very high Cr_2O_3 contents in ferroan olivines (mean $Cr_2O_3 = 0.36 \pm 0.06$ wt.%; Davidson et al., 2014b), like ALHA77307. Davidson et al. (2014b) also showed that, like ALHA77307, the matrix in DOM 08006 is composed of a highly unequilibrated mixtures of amorphous silicate, olivine, pyroxene, metal and sulfides. Apart from some signs of terrestrial weathering (e.g., Fe oxy-hydride needles), DOM 08006 does not exhibit any evidence of thermal metamorphism or aqueous alteration, and is mostly composed of a mixture of amorphous silicates, olivine, pyroxene, metal and sulfides (Davidson et al., 2014b). Initial data on DOM 08006 suggest that it is characterized by a very high abundance of presolar silicate grains (~210 ppm; Nittler et al., 2013).

Moreover, the Raman spectra of these three meteorites are also consistent with a classification as CO3.0. Bonal et al. (2007, 2016) show that the carbonaceous matter in these three meteorites is characterized by I_D/I_G ratios significantly lower than 1 ($I_D/I_G = 0.7$–0.8, Fig. S1), indicating that they belong to petrologic type 3.0.

2.2. Analytical methods

2.2.1. Optical Microscopy

Prior to analysis in the Cameca© NanoSIMS 50, the three thin sections were carbon-coated and examined using

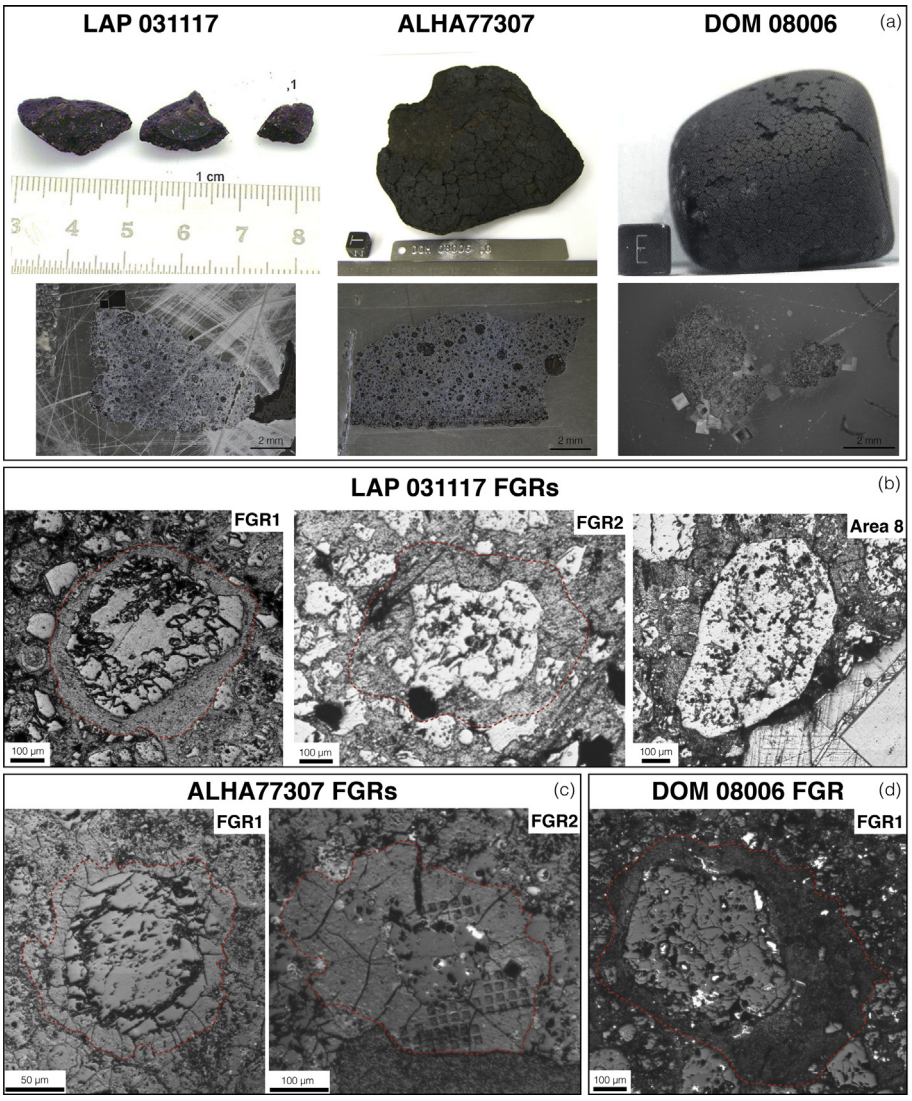

Fig. 1. (a) Photographs of the three CO3.0 chondrites LAP 031117, DOM 08006 and ALHA77307 (Meteorite photo credits: and overview photographs of the three thin-sections (LAP 031117,7; DOM 08006,13; ALHA77307,127). (b) Reflected light images of the two fine-grained rims (FGRs) and area 8 in LAP 031117. (c) Reflected light images of the two FGRs in ALHA77307. (d) Reflected light images of the FGR in DOM 08006. The red dashed lines indicate the border of the FGRs.

an Olympus© BH-2 petrographic microscope to locate dark fine-grained areas (both matrix and FGRs) for presolar grain searches. While many chondrules in these meteorites are surrounded by well-defined thin FGRs, we selected the five large rims (Fig. 1) in order to be able to map enough surface area with the NanoSIMS to have comparable counting statistics as the matrix.

2.2.2. NanoSIMS 50 Ion microprobe

Isotopically anomalous grains were located using the Cameca© NanoSIMS 50 ion microprobe at Washington University in St. Louis. We carried out raster ion imaging using a focused Cs^+ primary beam of ~1 pA, with a diameter of ~100 nm that was rastered over individual matrix or chondrule rim areas. Secondary ions of $^{12}C^-$, $^{13}C^-$, $^{16}O^-$, $^{17}O^-$ and $^{18}O^-$, as well as secondary electrons (SE), were simultaneously acquired in multicollection mode. To remove the carbon-coat and to implant primary ions into the fine-grained regions of interest, we first rastered a high beam current (~20 pA) over 12 × 12 µm^2 areas. Each measurement then consisted of 5–10 scans (or layers) of 10 × 10 µm^2 (256 × 256 pixels) areas rastered within the pre-sputtered region, with dwell times of 20,000 µs per pixel per scan. To avoid any mass shift between different layers, all mass peak positions were automatically calibrated based on the shift in $^{16}O^-$. The individual layers were then added together to make a single image for each component analyzed (^{12}C, ^{13}C, ^{16}O, ^{17}O, ^{18}O, and SE). The measurements were carried out in automated mapping mode, following predefined grid patterns of up to 30 measurements. We measured a total of 93,600 µm^2 in the matrix and FGRs of LAP 031117, ALHA77307 and DOM 08006 (66,200 µm^2; 10,800 µm^2 and 16,600 µm^2 respectively; Table 1). Carbon and oxygen isotopic compositions were

Table 1
Presolar grain abundances and total area measured in the matrix and fine-grained chondrule rims in the CO3.0 chondrites LAP 031117, ALHA77307 and DOM 08006.

		Total area measured (μm^2)	Number of O-anom grains	Number of C-anom grains	Presolar grain abundances (ppm)			
					O-anom. grains	Silicates	Oxides	C-anom. grains
LAP 031117	Matrix	37,300	88	11	177 ± 19	167 ± 18	10 ± 4	40 ± 10
	FGR 1	10,800	15	9	85 ± 23	77 ± 21	21 ± 15	66^{+30}_{-21}
	FGR 2	12,200	18	6	64 ± 15	64 ± 15	≤7[c]	45^{+30}_{-17}
	Area 8[a]	5,900	9	1	94^{+43}_{-31}	–	–	22^{+51}_{-18}
	Overall	66,200	130	27	150 ± 13	130 ± 13	9 ± 3	43 ± 8
ALHA77307	Matrix[b]	21,200	74	21	178 ± 21	171 ± 21	7 ± 4	62 ± 14
	FGR 1	10,800	5	2	54^{+37}_{-23}	–	–	66^{+88}_{-43}
	FGR 2[b]	6,300	25	5	245 ± 49	198 ± 43	48 ± 24	36^{+24}_{-15}
	Overall	38,300	104	28	162 ± 16	–	–	59 ± 13
DOM 08006	Matrix	12,500	51	6	227 ± 32	216 ± 31	11 ± 8	31^{+19}_{-12}
	FGR 1	4,100	4	0	58^{+46}_{-28}	–	–	≤24[c]
	Overall	16,600	55	6	160 ± 22	–	–	24^{+15}_{-10}
Overall CO3.0 chondrites		121,100	290	61	155 ± 9	138 ± 11	12 ± 3	47 ± 6

Notes. Errors on abundance estimates are 1σ.
[a] Area 8 is a possible FGR, see text for details.
[b] Based on the data from Bose et al. (2012).
[c] Upper limit estimate.

normalized to the average composition of matrix material, assuming solar bulk isotopic compositions ($^{17}O/^{16}O = 3.8 \times 10^{-4}$, $^{16}O/^{18}O = 2.0 \times 10^{-3}$ and $^{12}C/^{13}C = 89$). A grain was considered presolar if it fulfilled two conditions: (1) its isotopic compositions deviated from the average surrounding material by more than 4σ, and (2) the anomaly was present in at least three consecutive image layers.

The reported isotopic compositions should be considered lower limits; the true grain compositions are probably more anomalous, as dilution from surrounding isotopically normal grains has a significant effect on the measured isotopic compositions of presolar grains (Nguyen et al., 2007). This effect is most pronounced for the smallest grains, like the silicates, which have an average diameter of about 250–300 nm (e.g., Nguyen et al., 2007; Floss and Haenecour, 2016a) and for grains with depletions in ^{18}O and/or ^{17}O.

2.2.3. Scanning Auger Nanoprobe

Some of the identified carbon- and oxygen-anomalous grains were then further analyzed with the PHI 700 Auger Nanoprobe at Washington University in St. Louis to determine their elemental compositions and to clearly discriminate oxide from silicate grains. Prior to acquiring Auger spectra and/or elemental maps, the areas of interest were sputter cleaned by scanning a widely defocused 2 kV, 1 μm Ar^+ ion beam over a broad area (~2 mm^2) of the sample surface in order to remove atmospheric surface contamination. High-resolution secondary electron images were acquired to relocate precisely the presolar grains. Auger electron energy spectra of each relocated grain in LAP 031117 and DOM 08006 were then acquired at a primary beam accelerating voltage of 10 keV and a current of 0.25 nA in the energy range of 30–1730 eV. Quantitative elemental compositions were derived from the Auger spectra based on sensitivity factors derived from silicate standards (olivine grains with compositions ranging from Fo54 to Fo85 and a variety of pyroxene grains). These sensitivity factors and their relative uncertainties (in parentheses) are O: 0.194 (3.6%), Si: 0.121 (11.0%), Mg: 0.234 (9.4%), Fe: 0.150 (11.2%), Ca: 0.626 (10.8%), and Al: 0.160 (24.9%); see Stadermann et al. (2009) for a detailed description of the processing and quantification procedure of the Auger spectra. The most common contaminants observed in some spectra of O-anomalous grains were carbon and sulfur; these elements were not included in the quantification for O-anomalous grains when their concentrations were lower than 5 at.%. Because of charging issues, we were unable to obtain Auger spectra of the presolar grains identified in ALHA77307.

For a few selected presolar grains, we also acquired high-resolution elemental distribution maps (3×3 μm^2 or 5×5 μm^2; 256^2 pixels) at 10 keV and 10 nA for 3–25 scans, depending on the element being mapped (e.g., C, O, Mg, Al, Si, S, Ca, and Fe). The maps provide detailed qualitative information about the distribution of elements in the presolar grains of interest, and allow us to evaluate the possibility of contributions to the Auger spectra from surrounding grains.

Table 2
Oxygen isotopic compositions, elemental compositions and sizes of presolar silicate and oxide grains from the matrix and fine-grained chondrule rims in DOM 08006, ALHA77307 and LAP 031117.

Grain name	Sizes (nm^2)	$^{17}O/^{16}O$ ($\times10^{-4}$)	$^{18}O/^{16}O$ ($\times10^{-3}$)	Groups	O (at.%)	Si (at.%)	Mg (at.%)	Fe (at.%)	Ca (at.%)	Al (at.%)	Mineral phase
DOM 08006 Matrix (51 grains)											
DOM-7	310 × 310	3.5 ± 0.1	1.66 ± 0.03	3	–	–	–	–	–	–	–
DOM-8	195 × 350	5.9 ± 0.2	1.96 ± 0.03	1	–	–	–	–	–	–	–
DOM-9	235 × 235	5.3 ± 0.2	1.83 ± 0.04	1	67 ± 2	–	11 ± 1	–	–	22 ± 6	Spinel[a]
DOM-10	195 × 195	6 ± 0.3	1.94 ± 0.05	1	56 ± 2	10.6 ± 1.1	4.5 ± 0.4	28.4 ± 3.1	–	–	Silicate
DOM-11	195 × 195	6.3 ± 0.3	1.77 ± 0.05	1	58 ± 2	17.6 ± 1.9	6.4 ± 0.6	8.5 ± 0.9	3.6 ± 0.3	6.2 ± 1.5	Silicate
DOM-13	235 × 275	6.2 ± 0.2	1.35 ± 0.04	1	62 ± 2	14.5 ± 1.5	16.7 ± 1.5	6.6 ± 0.7	–	–	Silicate
DOM-14	195 × 195	5.3 ± 0.2	1.89 ± 0.05	1	62 ± 2	23.6 ± 2.5	5.9 ± 0.5	8.5 ± 0.9	–	–	Silicate
DOM-15	275 × 275	6 ± 0.3	1.87 ± 0.05	1	56 ± 2	14.6 ± 1.6	20.4 ± 1.9	8.6 ± 0.9	–	–	Silicate
DOM-16	235 × 235	7.9 ± 0.5	1.94 ± 0.08	1	70 ± 2	21.3 ± 2.3	0 ± 0	9.1 ± 1	–	–	Silicate
DOM-17	195 × 195	6 ± 0.3	1.99 ± 0.05	1	53 ± 1	14 ± 1.5	19.3 ± 1.8	13.5 ± 1.5	–	–	Silicate
DOM-18	195 × 195	5.3 ± 0.3	1.47 ± 0.05	1	57 ± 2	20.6 ± 2.2	10.5 ± 0.9	12.3 ± 1.3	–	–	Silicate
DOM-19	235 × 235	10.2 ± 0.4	1.29 ± 0.04	1	58 ± 2	12.6 ± 1.3	22.1 ± 2	7 ± 0.7	–	–	Silicate
DOM-20	195 × 195	6.4 ± 0.2	2.01 ± 0.04	1	–	–	–	–	–	–	–
DOM-21	195 × 195	5.4 ± 0.2	1.73 ± 0.04	1	57 ± 2	20.7 ± 2.2	3.4 ± 0.3	18.7 ± 2	–	–	Silicate
DOM-22	195 × 195	3.8 ± 0.2	2.47 ± 0.05	4	55 ± 1	11.2 ± 1.2	18.3 ± 1.7	15.2 ± 1.7	–	–	Silicate
DOM-23	235 × 235	23.1 ± 0.9	1.96 ± 0.08	1	51 ± 1	13.2 ± 1.4	3.4 ± 0.3	31.9 ± 3.5	–	–	Silicate
DOM-24	350 × 310	11.1 ± 0.6	0.93 ± 0.05	2	62 ± 2	20 ± 2.2	11 ± 1	7.1 ± 0.7	–	–	Silicate
DOM-26	235 × 235	7.7 ± 0.5	1.91 ± 0.08	1	–	–	–	–	–	–	–
DOM-27	235 × 235	5.6 ± 0.2	1.71 ± 0.04	1	56 ± 2	12.5 ± 1.3	13.6 ± 1.2	17.5 ± 1.9	–	–	Silicate
DOM-28	235 × 235	6.3 ± 0.2	2.07 ± 0.05	1	49 ± 1	12.1 ± 1.3	10.7 ± 1	28.4 ± 3.1	–	–	Silicate
DOM-29	270 × 275	5.8 ± 0.2	1.89 ± 0.04	1	65 ± 2	21.3 ± 2.3	3 ± 0.2	11.2 ± 1.2	–	–	Silicate
DOM-30	195 × 195	5.9 ± 0.2	1.95 ± 0.05	1	–	–	–	–	–	–	–
DOM-31	235 × 235	6.2 ± 0.2	1.37 ± 0.04	1	59 ± 2	8.9 ± 0.9	26.4 ± 2.4	5.6 ± 0.6	–	–	Silicate
DOM-32	235 × 235	5.5 ± 0.3	1.9 ± 0.06	1	57 ± 2	20.3 ± 2.2	4.5 ± 0.4	8 ± 0.8	–	10.2 ± 2.5	Silicate
DOM-33	195 × 195	6.4 ± 0.2	1.88 ± 0.05	1	56 ± 2	10.3 ± 1.1	10.8 ± 1	22.9 ± 2.5	–	–	Silicate
DOM-34	195 × 195	8.3 ± 0.7	1.75 ± 0.1	1	59 ± 2	11.5 ± 1.2	15 ± 1.4	14.8 ± 1.6	–	–	Silicate
DOM-35	235 × 235	4 ± 0.2	3.34 ± 0.07	4	60 ± 2	12.2 ± 1.3	8.6 ± 0.8	19.5 ± 2.1	–	–	Silicate
DOM-36	195 × 195	30 ± 1.1	2.04 ± 0.09	1	61 ± 2	19.1 ± 2.1	10.3 ± 0.9	10.1 ± 1.1	–	–	Silicate
DOM-37	235 × 235	6.5 ± 0.2	2.01 ± 0.05	1	59 ± 2	20.1 ± 2.2	7.1 ± 0.6	13.6 ± 1.5	–	–	Silicate
DOM-38	235 × 235	5.6 ± 0.2	1.92 ± 0.04	1	57 ± 2	21.2 ± 2.3	7 ± 0.6	15.3 ± 1.7	–	–	Silicate
DOM-39	275 × 275	6.4 ± 0.3	2.64 ± 0.07	4	52 ± 1	16 ± 1.7	16.6 ± 1.5	15.2 ± 1.7	–	–	Silicate
DOM-40	275 × 275	6.1 ± 0.4	1.82 ± 0.07	1	58 ± 2	10.4 ± 1.1	9.6 ± 0.9	9.5 ± 1	–	12.5 ± 3.1	Silicate
DOM-41	195 × 195	5.5 ± 0.2	2.05 ± 0.04	1	65 ± 2	16.8 ± 1.8	6.8 ± 0.6	11.2 ± 1.2	–	–	Silicate
DOM-42	275 × 275	5.4 ± 0.2	1.91 ± 0.05	1	59 ± 2	21.2 ± 2.3	7.3 ± 0.6	12.5 ± 1.4	–	–	Silicate
DOM-43	275 × 235	5.1 ± 0.2	2.02 ± 0.05	1	59 ± 2	15.3 ± 1.6	10.3 ± 0.9	15.3 ± 1.7	–	–	Silicate
DOM-44	235 × 235	5.9 ± 0.2	1.66 ± 0.04	1	58 ± 2	12.6 ± 1.3	17.8 ± 1.6	11.5 ± 1.2	–	–	Silicate
DOM-45	235 × 235	8.6 ± 0.2	2.01 ± 0.04	1	52 ± 1	13.7 ± 1.5	17.1 ± 1.6	17.1 ± 1.9	–	–	Silicate
DOM-46	195 × 195	5.4 ± 0.2	1.89 ± 0.04	1	53 ± 1	11.5 ± 1.2	18.8 ± 1.7	16.7 ± 1.8	–	–	Silicate
DOM-47	195 × 195	6.3 ± 0.3	1.82 ± 0.05	1	58 ± 2	21.6 ± 2.3	6.1 ± 0.5	14.1 ± 1.5	–	–	Silicate
DOM-48	195 × 195	5.3 ± 0.2	1.73 ± 0.03	1	57 ± 2	12.3 ± 1.3	9.8 ± 0.9	20.9 ± 2.3	–	–	Silicate
DOM-49	235 × 195	5.3 ± 0.2	2.05 ± 0.04	1	59 ± 2	15.7 ± 1.7	9 ± 0.8	16.7 ± 1.8	–	–	Silicate

DOM-50	195 × 195	3.6 ± 0.2	2.56 ± 0.05	4	52 ± 1	11.1 ± 1.2	12.9 ± 1.2	24.3 ± 2.7	–	–	Silicate
DOM-51	310 × 275	14.2 ± 0.5	1.5 ± 0.05	1	49 ± 2	–	–	51 ± 6	–	–	Oxide
DOM-52	195 × 195	7 ± 0.3	2.12 ± 0.05	1	58 ± 2	11.9 ± 1.3	19 ± 1.7	10.9 ± 1.2	–	–	Silicate
DOM-53	235 × 195	8.3 ± 0.2	1.91 ± 0.04	1	55 ± 1	16.8 ± 1.8	13.1 ± 1.2	15.2 ± 1.7	–	–	Silicate
DOM-54	235 × 235	7.6 ± 0.2	1.89 ± 0.04	1	54 ± 1	16.8 ± 1.8	6.3 ± 0.5	17.3 ± 1.9	5.6 ± 0.6	–	Silicate
DOM-56	235 × 235	5 ± 0.2	2.03 ± 0.04	1	57 ± 2	17.4 ± 1.9	12.1 ± 1.1	13.2 ± 1.4	–	–	Silicate
DOM-58	275 × 275	5.1 ± 0.2	1.93 ± 0.05	1	56 ± 2	14.5 ± 1.5	19.4 ± 1.8	7.7 ± 0.8	–	–	Silicate
DOM-59	310 × 390	11.6 ± 0.5	0.69 ± 0.03	2	50 ± 1	16.7 ± 1.8	19.5 ± 1.8	13 ± 1.4	–	–	Silicate
DOM-60	235 × 235	6 ± 0.2	2.06 ± 0.05	1	58 ± 2	13.2 ± 1.4	6.3 ± 0.5	22.6 ± 2.5	–	–	Silicate
DOM-61	195 × 160	5.6 ± 0.3	1.88 ± 0.05	1	58 ± 2	14.3 ± 1.5	5.6 ± 0.5	22.3 ± 2.4	–	–	Silicate
DOM 08006 FGR (4 grains)											
DOM-1	235 × 235	6 ± 0.3	2.1 ± 0.06	1	–	–	–	–	–	–	–
DOM-2	235 × 235	5.6 ± 0.3	1.87 ± 0.06	1	–	–	–	–	–	–	–
DOM-3	275 × 275	7.5 ± 0.4	1.25 ± 0.05	1	–	–	–	–	–	–	–
DOM-4	235 × 235	6.6 ± 0.4	1.45 ± 0.06	1	–	–	–	–	–	–	–
ALHA77307 FGR (5 grains)											
ALHA-1	470 × 470	5.6 ± 0.1	1.93 ± 0.03	1	–	–	–	–	–	–	–
ALHA-2	550 × 550	4.6 ± 0.1	2.00 ± 0.03	1	–	–	–	–	–	–	–
ALHA-3	310 × 310	4.8 ± 0.2	2.02 ± 0.04	1	–	–	–	–	–	–	–
ALHA-4	270 × 270	29.4 ± 1.7	1.9 ± 0.1	1	–	–	–	–	–	–	–
ALHA-5	310 × 310	3.6 ± 0.3	2.46 ± 0.09	4	–	–	–	–	–	–	–
LAP 031117 matrix (88 grains)											
LAP-1	155 × 195	8.7 ± 0.2	2.03 ± 0.02	1	58.4 ± 2.1	23.6 ± 2.5	–	18 ± 2	–	–	Silicate
LAP-2	195 × 195	6.1 ± 0.1	1.48 ± 0.02	1	56 ± 2	12.5 ± 1.3	13.5 ± 1.2	18 ± 2	–	–	Silicate
LAP-3	195 × 195	5 ± 0.1	1.91 ± 0.02	1	55.4 ± 1.9	15.3 ± 1.6	11.4 ± 1	17.9 ± 2	–	–	Silicate
LAP-4	195 × 195	5.1 ± 0.1	1.65 ± 0.03	1	57.2 ± 2	13.7 ± 1.5	13.9 ± 1.3	15.2 ± 1.7	–	–	Silicate
LAP-7	155 × 195	6 ± 0.3	2.16 ± 0.04	1	–	–	–	–	–	–	–
LAP-8	155 × 155	13.9 ± 0.9	2.1 ± 0.1	1	–	–	–	–	–	–	–
LAP-9	195 × 155	4 ± 0.1	2.38 ± 0.04	4	57 ± 2	26.2 ± 2.8	–	16.8 ± 1.8	–	–	Silicate
LAP-10	390 × 300	7 ± 0.3	0.68 ± 0.03	2	63.8 ± 2.2	19.9 ± 2.1	16.3 ± 1.5	–	–	–	Silicate
LAP-11	390 × 310	6.9 ± 0.4	1.4 ± 0.06	1	56.8 ± 2	12.9 ± 1.4	16.8 ± 1.5	13.6 ± 1.5	–	–	Silicate
LAP-12	195 × 350	5.3 ± 0.1	2.01 ± 0.03	1	54.9 ± 1.9	16.6 ± 1.8	12.8 ± 1.2	15.7 ± 1.7	–	–	Silicate
LAP-13	235 × 235	5.4 ± 0.1	1.98 ± 0.02	1	61.6 ± 2.2	10.7 ± 1.1	–	27.8 ± 3.1	–	–	Silicate
LAP-14	235 × 195	5.1 ± 0.1	2.11 ± 0.03	1	56 ± 2	13.8 ± 1.5	8.5 ± 0.7	21.7 ± 2.4	–	–	Silicate
LAP-15	195 × 195	5.2 ± 0.2	1.91 ± 0.03	1	52.3 ± 1.8	16.2 ± 1.7	9.1 ± 0.8	22.4 ± 2.5	–	–	Silicate
LAP-16	235 × 195	9.1 ± 0.4	1.81 ± 0.05	1	68.5 ± 2.4	21.9 ± 2.4	9.5 ± 0.8	–	–	–	Silicate
LAP-17	275 × 235	4.9 ± 0.1	1.96 ± 0.02	1	58.1 ± 2	16.5 ± 1.8	11.4 ± 1	13.9 ± 1.5	–	–	Silicate
LAP-18	235 × 195	9.1 ± 0.2	1.96 ± 0.03	1	65 ± 2.3	–	9.5 ± 0.8	25.5 ± 2.8	–	–	Oxide
LAP-19	195 × 155	5.8 ± 0.3	1.85 ± 0.05	1	73.9 ± 2.6	–	–	26.1 ± 2.9	–	–	Oxide
LAP-20	235 × 195	6.1 ± 0.2	1.93 ± 0.04	1	57.7 ± 2	12.7 ± 1.3	6.3 ± 0.5	21.3 ± 2.3	–	–	Silicate
LAP-22	195 × 195	5.5 ± 0.2	2.04 ± 0.04	1	53.6 ± 1.9	10.2 ± 1.1	–	36.3 ± 4	–	–	Silicate
LAP-23	195 × 195	5.9 ± 0.7	1.91 ± 0.12	1	46.8 ± 1.6	14.3 ± 1.5	7.7 ± 0.7	31.1 ± 3.4	–	–	Silicate
LAP-24	350 × 230	5.3 ± 0.1	1.97 ± 0.03	1	51.5 ± 1.8	12.1 ± 1.3	–	36.4 ± 4	–	–	Silicate
LAP-25	390 × 195	5 ± 0.1	2.01 ± 0.03	1	57.8 ± 2	11.8 ± 1.2	–	10.4 ± 1.1		20 ± 4.9	Silicate
LAP-26	545 × 195	5.3 ± 0.3	2.08 ± 0.06	1	54.3 ± 1.9	15.9 ± 1.7	8.3 ± 0.7	21.5 ± 2.4	–	–	Silicate

(*continued on next page*)

Table 2 (*continued*)

Grain name	Sizes (nm^2)	$^{17}O/^{16}O$ ($\times10^{-4}$)	$^{18}O/^{16}O$ ($\times10^{-3}$)	Groups	O (at.%)	Si (at.%)	Mg (at.%)	Fe (at.%)	Ca (at.%)	Al (at.%)	Mineral phase
LAP-27d	500 × 230	4.9 ± 0.1	1.83 ± 0.02	1	57.3 ± 2	14.4 ± 1.5	–	28.3 ± 3.1	–	–	Silicate
LAP-28	390 × 500	7.5 ± 0.2	1.33 ± 0.03	1	61.9 ± 2.2	15.2 ± 1.6	22.9 ± 2.1	–	–	–	Silicate
LAP-30	270 × 270	9.2 ± 0.2	1.7 ± 0.03	1	66.5 ± 2.3	–	10.7 ± 1	–	–	22.8 ± 5.6	Oxide
LAP-33	350 × 350	5.7 ± 0.1	1.65 ± 0.03	1	57.7 ± 2	12.9 ± 1.4	10.8 ± 1	18.6 ± 2	–	–	Silicate
LAP-35	430 × 235	5.5 ± 0.1	1.63 ± 0.02	1	48.6 ± 1.7	11 ± 1.2	9.3 ± 0.8	31.2 ± 3.4	–	–	Silicate
LAP-36	390 × 235	4.6 ± 0.1	2.68 ± 0.04	4	66.5 ± 2.3	22.6 ± 2.4	10.9 ± 1	–	–	–	Silicate
LAP-66	430 × 235	6 ± 0.1	1.96 ± 0.02	1	–	–	–	–	–	–	–
LAP-68	390 × 470	4.8 ± 0.1	2.01 ± 0.02	1	45.9 ± 1.6	18.6 ± 2	8.5 ± 0.7	27 ± 3	–	–	Silicate?
LAP-69	390 × 390	3.8 ± 0.1	2.51 ± 0.03	4	–	–	–	–	–	–	–
LAP-70	235 × 235	5.5 ± 0.2	2 ± 0.04	1	46.7 ± 1.6	13.8 ± 1.5	9.1 ± 0.8	29.7 ± 3.3	–	–	Silicate
LAP-71	235 × 235	5 ± 0.2	2.01 ± 0.04	1	49.3 ± 1.7	10.1 ± 1.1	9.6 ± 0.9	25.9 ± 2.9	–	5 ± 1.2	Silicate
LAP-72	235 × 310	6.3 ± 0.2	2 ± 0.04	1	51.1 ± 1.8	7.8 ± 0.8	3.3 ± 0.3	28 ± 3.1	–	4.9 ± 1.2	Silicate?
LAP-73	275 × 275	6.1 ± 0.3	1.35 ± 0.04	1	54 ± 1.9	17.5 ± 1.9	8.8 ± 0.8	13.5 ± 1.5	–	6.1 ± 1.5	Silicate
LAP-74	195 × 195	5.5 ± 0.2	1.99 ± 0.05	1	53.7 ± 1.9	14.8 ± 1.6	8.9 ± 0.8	17.6 ± 1.9	2.9 ± 0.3	–	Silicate
LAP-75	195 × 195	5.2 ± 0.2	1.79 ± 0.04	1	–	–	–	–	–	–	–
LAP-76	310 × 310	7.8 ± 0.3	1.8 ± 0.04	1	78.7 ± 2.8	–	10.8 ± 1	10.5 ± 1.1	–	–	Oxide
LAP-77	235 × 235	7.2 ± 0.3	1.94 ± 0.04	1	51.9 ± 1.8	15.8 ± 1.7	13.8 ± 1.2	18.5 ± 2	–	–	Silicate
LAP-78	390 × 390	5.3 ± 0.2	1.88 ± 0.04	1	56.8 ± 2	14.1 ± 1.5	11.2 ± 1	17.9 ± 2	–	–	Silicate
LAP-79	310 × 275	5.4 ± 0.2	1.97 ± 0.04	1	62.7 ± 2.2	19 ± 2	8.9 ± 0.8	9.4 ± 1	–	–	Silicate
LAP-80	235 × 235	5.4 ± 0.3	1.9 ± 0.05	1	61.7 ± 2.2	16.5 ± 1.8	6.7 ± 0.6	15.1 ± 1.6	–	–	Silicate
LAP-81	255 × 255	12 ± 0.4	1.52 ± 0.04	1	61.9 ± 2.2	10.9 ± 1.1	20.8 ± 1.9	5.7 ± 0.6	–	–	Olivine[a]
LAP-82	310 × 310	12.4 ± 0.3	2.08 ± 0.04	1	60.9 ± 2.1	20 ± 2.2	6.8 ± 0.6	7.4 ± 0.8	4.9 ± 0.5	–	Silicate
LAP-83	275 × 275	6.4 ± 0.2	1.62 ± 0.04	1	46.5 ± 1.6	15.7 ± 1.7	9.3 ± 0.8	26.7 ± 2.9	1.9 ± 0.2	–	Silicate
LAP-85	350 × 195	4.9 ± 0.2	2.02 ± 0.04	1	55.1 ± 1.9	–	7.6 ± 0.7	14 ± 1.5	–	23.3 ± 5.8	Oxide
LAP-86	310 × 273	5.7 ± 0.2	1.97 ± 0.04	1	49 ± 1.7	11.4 ± 1.2	8 ± 0.7	26.4 ± 2.9	–	5.3 ± 1.3	Silicate
LAP-87	235 × 235	7.9 ± 0.3	1.79 ± 0.05	1	59.6 ± 2.1	–	8.8 ± 0.8	6.9 ± 0.7	–	24.7 ± 6.1	Oxide
LAP-88	195 × 195	6.3 ± 0.2	1.89 ± 0.04	1	54.4 ± 1.9	8.9 ± 0.9	10.1 ± 0.9	11.7 ± 1.3	–	15 ± 3.7	Silicate?
LAP-89	350 × 350	4.1 ± 0.1	2.29 ± 0.04	4	55 ± 1.9	15.8 ± 1.7	4.2 ± 0.3	18.3 ± 2	–	6.7 ± 1.6	Silicate
LAP-90	315 × 315	8.7 ± 1	1.93 ± 0.15	1	57.7 ± 2	15.9 ± 1.7	19.6 ± 1.8	6.8 ± 0.7	–	–	Silicate
LAP-92	315 × 315	5 ± 0.2	2.03 ± 0.04	1	–	–	–	–	–	–	–
LAP-93	350 × 350	5.1 ± 0.2	1.99 ± 0.04	1	47.1 ± 1.6	17.7 ± 1.9	11.7 ± 1	21.4 ± 2.3	2 ± 0.2	–	Silicate
LAP-94	275 × 275	4.9 ± 0.2	1.96 ± 0.04	1	51.3 ± 1.8	17.2 ± 1.8	6 ± 0.5	23.3 ± 2.6	2.2 ± 0.2	–	Silicate
LAP-95	310 × 310	6.8 ± 0.3	1.38 ± 0.04	1	–	–	–	–	–	–	–
LAP-96	275 × 275	4.2 ± 0.2	1.69 ± 0.04	1	–	–	–	–	–	–	–
LAP-97	270 × 240	5.1 ± 0.2	2.03 ± 0.05	1	–	–	–	–	–	–	–
LAP-98	270 × 270	6.7 ± 0.3	2.1 ± 0.05	1	57.8 ± 2	16.5 ± 1.8	8.9 ± 0.8	7.1 ± 0.7	3.7 ± 0.3	6 ± 1.4	Silicate
LAP-99	390 × 390	3.4 ± 0.1	1.96 ± 0.04	3	–	–	–	–	–	–	–
LAP-100	390 × 315	6 ± 0.2	1.64 ± 0.04	1	68.4 ± 2.4	17.3 ± 1.9	14.3 ± 1.3	–	–	–	Silicate
LAP-101	310 × 270	5 ± 0.2	1.8 ± 0.04	1	54.9 ± 1.9	19.7 ± 2.1	6.9 ± 0.6	18.5 ± 2	–	–	Silicate
LAP-139	235 × 235	3.9 ± 0.3	2.63 ± 0.07	4	–	–	–	–	–	–	–
LAP-140	235 × 270	6.9 ± 0.3	1.86 ± 0.04	1	51.8 ± 1.8	15.7 ± 1.7	13.1 ± 1.2	19.4 ± 2.1	–	–	Silicate
LAP-142	235 × 235	12.4 ± 0.4	1.74 ± 0.05	1	61.1 ± 2.1	10.7 ± 1.1	13.9 ± 1.3	9.3 ± 1	5 ± 0.5	–	Silicate
LAP-143	250 × 250	6.8 ± 0.3	2.03 ± 0.05	1	58.1 ± 2	13 ± 1.4	5.2 ± 0.4	20 ± 2.2	–	–	Silicate
LAP-144	270 × 310	5.3 ± 0.4	1.4 ± 0.06	1	56.1 ± 2	12.6 ± 1.3	4.1 ± 0.3	16.2 ± 1.8	–	7.3 ± 1.8	Silicate
LAP-145	275 × 275	5.3 ± 0.2	1.95 ± 0.05	1	49.3 ± 1.7	16.4 ± 1.8	9.8 ± 0.9	24.5 ± 2.7	–	–	Silicate

LAP-146	235 × 235	10.3 ± 0.4	1.86 ± 0.05	1	57.9 ± 2	14.9 ± 1.6	19.5 ± 1.8	7.7 ± 0.8	–	–	Silicate
LAP-147	200 × 200	6.5 ± 0.4	1.96 ± 0.06	1	56.9 ± 2	12.9 ± 1.4	12.6 ± 1.1	15.2 ± 1.7	–	–	Silicate
LAP-148	310 × 310	6 ± 0.3	2.05 ± 0.06	1	54.9 ± 1.9	16.7 ± 1.8	6.5 ± 0.6	17.1 ± 1.9	–	–	Silicate
LAP-150	230 × 230	6.9 ± 0.3	1.96 ± 0.05	1	55.4 ± 1.9	11.2 ± 1.2	4.3 ± 0.4	20.6 ± 2.3	–	5.2 ± 1.2	Silicate
LAP-151	315 × 315	5.9 ± 0.3	2.07 ± 0.05	1	55.4 ± 1.9	14.4 ± 1.5	6.7 ± 0.6	13.2 ± 1.4	–	10.3 ± 2.5	Silicate
LAP-152	315 × 315	15 ± 1.6	1.85 ± 0.15	1	61.1 ± 2.1	19.9 ± 2.1	11.2 ± 1	7.8 ± 0.8	–	–	Silicate
LAP-153	280 × 280	3.8 ± 0.3	1.51 ± 0.06	3	63.7 ± 2.2	–	–	36.3 ± 4	–	–	Oxide
LAP-154	270 × 270	8.3 ± 0.5	1.76 ± 0.07	1	63.3 ± 2.2	18.2 ± 2	5.1 ± 0.4	13.4 ± 1.5	–	–	Silicate
LAP-155	235 × 235	4.8 ± 0.3	1.63 ± 0.05	1	55.6 ± 2	15.1 ± 1.6	13.6 ± 1.2	15.7 ± 1.7	–	–	Silicate
LAP-156	310 × 275	8.6 ± 0.4	1.47 ± 0.05	1	56.8 ± 2	15.6 ± 1.7	12.6 ± 1.1	15.1 ± 1.6	–	–	Silicate
LAP-157	230 × 200	8.3 ± 0.3	1.9 ± 0.04	1	59.7 ± 2.1	11.7 ± 1.2	12.9 ± 1.2	15.7 ± 1.7	–	–	Silicate
LAP-158	230 × 230	5.8 ± 0.3	2.07 ± 0.05	1	62.1 ± 2.2	21.6 ± 2.3	–	8.6 ± 0.9	–	7.6 ± 1.8	Silicate
LAP-159	275 × 235	5.2 ± 0.3	2.06 ± 0.05	1	56.7 ± 2	15.1 ± 1.6	5.8 ± 0.5	15.7 ± 1.7	–	6.6 ± 1.6	Silicate
LAP-160	315 × 315	3.6 ± 0.4	4.97 ± 0.16	4	66.5 ± 2.3	19.7 ± 2.1	–	13.8 ± 1.5	–	–	Silicate
LAP-161	275 × 275	13.6 ± 0.5	1.75 ± 0.05	1	57.7 ± 2	13.5 ± 1.4	8.3 ± 0.7	15.5 ± 1.7	–	5 ± 1.2	Silicate
LAP-162	320 × 320	3.7 ± 0.2	2.86 ± 0.07	4	55 ± 1.9	12.4 ± 1.3	13.7 ± 1.2	8.4 ± 0.9	–	10.5 ± 2.6	Silicate
LAP-163	230 × 270	6.7 ± 0.3	2.05 ± 0.05	1	58.1 ± 2	17.5 ± 1.9	10 ± 0.9	8.4 ± 0.9	6 ± 0.6	–	Silicate
LAP-164	280 × 280	6.5 ± 0.3	2.81 ± 0.06	4	52.9 ± 1.9	7.6 ± 0.8	15 ± 1.4	21.4 ± 2.3	3 ± 0.3	–	Silicate?
LAP-165	200 × 200	7.7 ± 0.4	1.9 ± 0.07	1	51.9 ± 1.8	18.3 ± 2	11.1 ± 1	10.2 ± 1.1	2.1 ± 0.2	6.5 ± 1.6	Silicate
LAP-166	230 × 230	6.1 ± 0.3	1.42 ± 0.05	1	60.8 ± 2.1	–	7.1 ± 0.6	8.6 ± 0.9	1.8 ± 0.1	21.6 ± 5.3	Oxide
LAP-53	195 × 195	2.8 ± 0.4	2.81 ± 0.2	4	73.8 ± 2.6	26.2 ± 2.8	–	–	–	–	SiO_2
LAP 031117 FGRs (42 grains)											
LAP-38	275 × 195	4.5 ± 0.3	2.51 ± 0.07	4	–	–	–	–	–	–	–
LAP-39	195 × 195	7.3 ± 0.3	1.92 ± 0.04	1	57.7 ± 2	13.7 ± 1.5	13.2 ± 1.2	15.4 ± 1.7	–	–	Silicate
LAP-42	430 × 470	6.9 ± 0.2	1.15 ± 0.03	1	66.3 ± 2.3	–	9 ± 0.8	–	–	24.6 ± 6.1	Oxide
LAP-44	390 × 390	5.6 ± 0.2	1.91 ± 0.04	1	–	–	–	–	–	–	–
LAP-45	195 × 156	6.9 ± 0.3	2.06 ± 0.05	1	55.4 ± 1.9	7.2 ± 0.7	14.2 ± 1.3	23.2 ± 2.5	–	–	Silicate
LAP-46	195 × 156	6.8 ± 0.2	2.13 ± 0.04	1	50.3 ± 1.8	16.8 ± 1.8	13.2 ± 1.2	19.6 ± 2.1	–	–	Silicate
LAP-47	310 × 310	4.5 ± 0.2	1.74 ± 0.04	1	–	–	–	–	–	–	–
LAP-48	195 × 195	7.4 ± 0.3	1.89 ± 0.05	1	59.5 ± 2.1	16.1 ± 1.7	14 ± 1.3	10.4 ± 1.1	–	–	Silicate
LAP-49	195 × 195	4.4 ± 0.2	2.45 ± 0.04	4	53.6 ± 1.9	12.2 ± 1.3	13.9 ± 1.3	20.3 ± 2.2	–	–	Silicate
LAP-50	230 × 310	6.3 ± 0.2	1.85 ± 0.03	1	50.9 ± 1.8	16.3 ± 1.7	17.8 ± 1.6	15 ± 1.6			Silicate
LAP-51	195 × 230	23.5 ± 0.6	1.92 ± 0.05	1	54.6 ± 1.9	13.2 ± 1.4	11.1 ± 1	21.1 ± 2.3	–	–	Silicate
LAP-52	195 × 235	6.9 ± 0.3	1.89 ± 0.06	1	53.8 ± 1.9	14.1 ± 1.5	9.7 ± 0.9	11.2 ± 1.2	–	11.2 ± 2.7	Silicate
LAP-57	390 × 310	5.3 ± 0.2	1.57 ± 0.03	1	58 ± 2	19.1 ± 2.1	16.2 ± 1.5	6.7 ± 0.7	–	–	Silicate
LAP-58	155 × 270	5.2 ± 0.1	1.93 ± 0.02	1	–	–	–	–	–	–	–
LAP-103	780 × 780	38.5 ± 1.5	2.12 ± 0.1	1	–	–	–	–	–	–	Magnetite[a]
LAP-104	270 × 270	21.9 ± 1.6	2.3 ± 0.15	1	–	–	–	–	–	–	Silicate[a]
LAP-108	195 × 195	5.8 ± 0.3	1.9 ± 0.05	1	52.3 ± 1.8	10.1 ± 1.1	8.6 ± 0.8	23.4 ± 2.6	–	–	Silicate
LAP-109	230 × 230	3.6 ± 0.2	4.31 ± 0.07	4	57.6 ± 2	11.9 ± 1.3	5 ± 0.4	25.5 ± 2.8	–	–	Silicate
LAP-110	270 × 270	7.5 ± 0.7	1.63 ± 0.1	1	64.8 ± 2.3	11.6 ± 1.2		23.6 ± 2.6	–	–	Silicate
LAP-111	350 × 350	7 ± 0.3	1.1 ± 0.03	1	55.2 ± 1.9	10.1 ± 1.1	8.8 ± 0.8	25.9 ± 2.9	–	–	Silicate
LAP-112	270 × 270	6.5 ± 0.2	1.94 ± 0.04	1	60.4 ± 2.1	17.3 ± 1.9	8.8 ± 0.8	13.5 ± 1.5	–	–	Silicate
LAP-113	270 × 270	5.7 ± 0.2	1.84 ± 0.04	1	60.6 ± 2.1	17.8 ± 1.9	10.3 ± 0.9	11.2 ± 1.2	–	–	Silicate
LAP-114	270 × 270	5.6 ± 0.2	2.09 ± 0.04	1	54.2 ± 1.9	12.8 ± 1.4	12.4 ± 1.1	20.6 ± 2.3	–	–	Silicate
LAP-116	230 × 230	5.6 ± 0.3	1.88 ± 0.05	1	55.9 ± 2	28.6 ± 3.1	4.6 ± 0.4	10.9 ± 1.2	–	–	Silicate
LAP-117	270 × 270	4.1 ± 0.2	2.66 ± 0.06	4	61.9 ± 2.2	23.2 ± 2.5	6 ± 0.5	8.8 ± 0.9	–	–	Silicate

(*continued on next page*)

Table 2 (*continued*)

Grain name	Sizes (nm^2)	$^{17}O/^{16}O$ ($\times 10^{-4}$)	$^{18}O/^{16}O$ ($\times 10^{-3}$)	Groups	O (at.%)	Si (at.%)	Mg (at.%)	Fe (at.%)	Ca (at.%)	Al (at.%)	Mineral phase
LAP-118	310 × 310	5.5 ± 0.2	1.41 ± 0.04	1	53.3 ± 1.9	22 ± 2.4	6.4 ± 0.6	18.3 ± 2	–	–	Silicate
LAP-119	310 × 310	5.4 ± 0.2	2.02 ± 0.04	1	54.6 ± 1.9	21.6 ± 2.3	7.2 ± 0.6	16.6 ± 1.8	–	–	Silicate
LAP-120	270 × 270	7.2 ± 0.4	1.99 ± 0.06	1	50.8 ± 1.8	16.5 ± 1.8	10 ± 0.9	22.7 ± 2.5	–	–	Silicate
LAP-121	235 × 235	7.3 ± 0.3	1.97 ± 0.05	1	51.9 ± 1.8	12.4 ± 1.3	15.4 ± 1.4	20.3 ± 2.2	–	–	Silicate
LAP-122	310 × 310	6 ± 0.2	1.99 ± 0.04	1	51 ± 1.8	13.1 ± 1.4	10.9 ± 1	19.6 ± 2.1	–	5.4 ± 1.3	Silicate
LAP-123	235 × 234	6.4 ± 0.2	1.6 ± 0.04	1	60.8 ± 2.1	6.4 ± 0.7	3.1 ± 0.2	24.7 ± 2.7	–	5 ± 1.2	Silicate?
LAP-124	195 × 195	6.5 ± 0.4	1.79 ± 0.06	1	51.4 ± 1.8	18.2 ± 2	12.6 ± 1.1	17.8 ± 1.9	–	–	Silicate
LAP-54[b]	200 × 200	3.9 ± 0.2	3.07 ± 0.05	4	45.7 ± 1.6	15.8 ± 1.7	11.4 ± 1	27.2 ± 3	–	–	Silicate
LAP-55[b]	150 × 180	5.1 ± 0.1	2.04 ± 0.03	1	56.8 ± 2	13.3 ± 1.4	11.8 ± 1.1	18.1 ± 2	–	–	Silicate
LAP-56[b]	250 × 200	5.1 ± 0.2	1.93 ± 0.03	1	49.9 ± 1.7	19 ± 2	13 ± 1.2	18.2 ± 2	–	–	Silicate
LAP-126[b]	235 × 235	10.2 ± 0.4	2.08 ± 0.06	1	51.5 ± 1.8	17.1 ± 1.8	7.3 ± 0.6	24.2 ± 2.7	–	–	Silicate
LAP-128[b]	250 × 250	12.2 ± 0.5	1.72 ± 0.06	1	59.3 ± 2.1	11.6 ± 1.2	8.9 ± 0.8	20.2 ± 2.2	–	–	Silicate
LAP-129[b]	235 × 235	7.1 ± 0.2	1.71 ± 0.04	1	49 ± 1.7	12 ± 1.3	5.2 ± 0.4	33.7 ± 3.7	–	–	Silicate
LAP-130[b]	235 × 235	4.6 ± 0.1	1.69 ± 0.03	1	60.4 ± 2.1	19.7 ± 2.1	5.1 ± 0.4	14.8 ± 1.6	–	–	Silicate
LAP-132[b]	270 × 270	5.6 ± 0.2	2.08 ± 0.05	1	49.5 ± 1.7	14.6 ± 1.6	9.8 ± 0.9	26.2 ± 2.9	–	–	Silicate
LAP-135[b]	250 × 250	4.7 ± 0.2	2.02 ± 0.04	1	52.5 ± 1.8	11.9 ± 1.3	9.6 ± 0.9	26 ± 2.9	–	–	Silicate

Notes. Errors are 1σ.
[a] Mineralogy based on transmission electron microscopy analysis (Zega et al., 2017, 2015, 2014).
[b] Grain identified in another possible FGR (Area 8). See text for details.

2.2.4. Electron probe micro-analysis

We also acquired X-ray elemental maps and determined average major- and minor-element concentrations by EPMA (electron probe microanalyses) in several distinct matrix areas and FGRs in LAP 031117 and ALHA77307 using the JEOL JXA-8200 electron microprobe at Washington University in St. Louis. High-resolution backscattered electron (BSE) imaging and X-ray map analysis were also used to characterize the texture and structure of a chondrule rim (FGR 2) in ALHA77307. The major-element concentrations were determined using an accelerating voltage of 15 kV, a probe current of 25 nA and a beam size of about 10 μm. See Seddio et al. (2014) for additional details about the measurement procedure.

2.2.5. Focused-Ion beam lift-out and transmission electron microscopy

Electron transparent cross sections of several fine-grained areas (including both matrix and FGRs) and several presolar grains were prepared via focused ion beam (FIB) lift-out for detailed structural and chemical analysis with transmission electron microscopy (TEM). Several FIB-SEMs were used in the course of this work, including: the FEI Quanta 3-D instrument at Washington University in St. Louis, the FEI Nova 200 dual beam FIB-SEM at Arizona State University, and the FEI Quanta 3D at NASA Johnson Space Center (Houston, TX). In general, the procedures used to prepare the FIB sections are similar to those described in Zega et al. (2007, 2015).

The FIB sections were examined with several transmission electron microscopes. These include the 200 keV JEOL 2200FS at the Naval Research Laboratory; the 200 keV JEOL 2500SE at NASA Johnson Space Center, the 200 keV JEOL ARM at Arizona State University, and the JEOL 2000FX at Washington University. The JEOL 2000FX is equipped with a NORAN ultra-thin window energy dispersive X-ray spectrometer (EDXS). The 2200FS, 2500SE, and ARM are equipped with thin window, Li-drifted Si, energy-dispersive X-ray spectrometers (EDS) and bright-field (BF) and dark-field (DF) scanning TEM (STEM) detectors.

2.2.6. Raman spectroscopy

Raman spectroscopy was used to obtain information about the structure and heating history of the carbonaceous matter (e.g., insoluble organic matter) in fine-grained areas of the LAP 031117 and DOM 08006 meteorites. The spectra were acquired in areas previously presputtered for the NanoSIMS measurements. We used the Renishaw inVia© Raman imaging system at Washington University in St. Louis, with a laser wavelength of 532 nm for excitation that was condensed by a long working distance 100 × objective (NA = 0.8) to a spot at the sample of less than <1 μm in size and laser power of 2.5 mW. The spectra were acquired around the two carbon peaks in a spectral window of 1000–2000 Δcm^{-1}. Carbonaceous matter in meteorites exhibits two first-order main carbon bands: the D-band (D for disordered carbon) at 1332 cm^{-1} and the G-band (G for graphitic carbon) at 1582 cm^{-1}. Previous studies (Bonal et al., 2006, 2007) have shown that the ratio of the relative

Table 3
Carbon isotopic compositions and sizes of C-anomalous grains identified in DOM 08006, ALHA77307 and LAP 031117.

Grain name	Size (nm^2)	$^{12}C/^{13}C$
DOM 08006 Matrix (6 grains)		
DOM-5	195 × 195	62.9 ± 2.2
DOM-6	390 × 390	17.4 ± 0.4
DOM-12	273 × 273	64.6 ± 1.8
DOM-25	312 × 312	6.4 ± 0.1
DOM-55	195 × 234	62.4 ± 2.5
DOM-57	234 × 234	63 ± 3
ALHA77307 FGR 1 (2 grains)		
ALHA-6	391 × 273	53 ± 8
ALHA-7	781 × 781	22 ± 1
LAP 031117 Matrix (11 grains)		
LAP-5	351 × 273	101.4 ± 2.4
LAP-6	351 × 273	65.6 ± 0.9
LAP-29	156 × 234	71.6 ± 2.8
LAP-31	850 × 420	62.6 ± 0.3
LAP-32	585 × 390	58.5 ± 0.9
LAP-34	468 × 507	138.0 ± 4.6
LAP-84	273 × 273	73.0 ± 2.6
LAP-91	351 × 351	66.2 ± 2.0
LAP-141	546 × 546	537 ± 24
LAP-149	858 × 897	1.41 ± 0.01
LAP-167	234 × 234	22.8 ± 0.9
LAP 031117 FGRs (16 grains)		
LAP-37	273 × 663	68.0 ± 1.1
LAP-41	234 × 234	60.8 ± 2.3
LAP-43	390 × 429	59.3 ± 1.2
LAP-59	234 × 273	60.5 ± 2.5
LAP-60	195 × 195	62.0 ± 5.0
LAP-61	234 × 195	52.0 ± 4.2
LAP-62	234 × 273	62.9 ± 4.0
LAP-63	234 × 234	63.7 ± 2.3
LAP-64	234 × 156	60.7 ± 5.4
LAP-102	390 × 390	62.9 ± 4.08
LAP-115	312 × 312	59.6 ± 2.7
LAP-125	312 × 312	112.9 ± 4.5
LAP-136	312 × 312	72 ± 4
LAP-137	273 × 273	74 ± 4
LAP-138	234 × 234	71 ± 3
LAP-134[a]	351 × 351	65.2 ± 1.5

Notes. Errors are 1σ.
[a] Grains identified in another possible FGR (Area 8). See text for details.

heights of the D- and G-bands provides direct information on the degree of structural order of the carbonaceous matter.

3. RESULTS

3.1. Isotopic compositions, sizes and chemistries of presolar grains identified in LAP 031117, ALHA77307 and DOM 08006

As shown in Fig. 1, we searched for presolar grains in nine (seven matrix areas and two FGRs) and six (five matrix areas and one FGRs) individual fine-grained regions in LAP 031117 and DOM 08006, respectively (Fig. 1). We also analyzed an additional FGR in ALHA77307 to compare with data from Bose et al. (2012).

We identified a total of 190 O-anomalous presolar grains in the matrix regions and FGRs of LAP 031117, ALHA77307 and DOM 08006. The elemental and isotopic compositions and sizes of the grains are presented in Table 2 (O-anomalous grains) and Table 3 (C-anomalous grains). Most of the O-anomalous grains (163 grains) exhibit excesses in ^{17}O relative to solar and have subsolar to solar $^{18}O/^{16}O$ ratios (Fig. 2) and belong to Group 1, based on the classification scheme proposed by Nittler et al. (1997). Five grains are characterized by both excesses in ^{17}O and depletions in ^{18}O relative to solar, and belong to Group 2. Nineteen other grains exhibit enrichments in ^{18}O relative to solar and belong to Group 4, and three grains belong to Group 3 with depletions in ^{17}O and ^{18}O relative to solar (Fig. 2).

Of the 190 O-anomalous grains, 160 were analyzed with the Auger Nanoprobe to determine their elemental compositions. The remaining 30 O-anomalous grains could not be analyzed either due to charging issues or because they could not be precisely relocated. While we do not have structural information for most of the presolar grains identified in this study, we use the silicate and oxide mineral terminology (e.g., olivine and pyroxene; corundum, spinel, and hibonite) to designate presolar grains with elemental compositions similar to these different phases.

The Auger analysis revealed that 148 grains (~92%) are ferromagnesian silicates, one grain (<1%) has a composition consistent with silica (SiO_2; LAP-53; Haenecour et al., 2013b) and 12 are oxide grains (~8%), including six spinel-like oxides, five Fe-rich oxides (including one grain whose stoichiometry is consistent with a wüstite-like composition) and one non-stoichiometric hibonite-like grain. Transmission electron microscopy analysis of two oxide grains in LAP 031117 and DOM 08006 (LAP-103 and DOM-9) confirmed that grain LAP-103 is a magnetite (Fe_3O_4) grain, representing the first definitive identification of a presolar magnetite grain (Zega et al., 2015), and DOM-9 is a polycrystalline Cr-rich spinel (Zega et al., 2017). Based on the number of presolar silicate and oxide grains identified in LAP 031117, DOM 08006 and ALHA77307, we calculated an overall silicate-to-oxide ratio of 12 ± 4 (22^{+29}_{-15} in DOM 08006, 10 ± 3 in LAP 031117 and 11^{+7}_{-5} in ALHA77307; the ratio for ALHA77307 is based on data from Bose et al. (2012). As reported in Table 2, the sizes of the presolar silicate and oxide grains identified range from 150 to 780 nm, with mean diameters of about 260 nm and 320 nm, respectively, for presolar silicate and oxide grains.

Beyond discrimination between silicate and oxide grains, Auger analysis of presolar O-anomalous grains can also be used to distinguish silicates with different stoichiometries (Stadermann et al., 2009). The nominal (Fe + Mg(+Ca))/Si atomic ratio is 1 for pyroxene ($(Mg,Fe)_2Si_2O_6$) and 2 for olivine ($(Mg,Fe)_2SiO_4$). Presolar silicates are classified as pyroxene-like or olivine-like if their (Fe + Mg(+Ca))/Si ratios fall within 1σ of the theoretical ratios for these minerals. Of the 148 ferromagnesian silicates, 21 grains have pyroxene-like elemental compositions and 34 grains have olivine-like compositions (Fig. 3). 83% of the pyroxene-

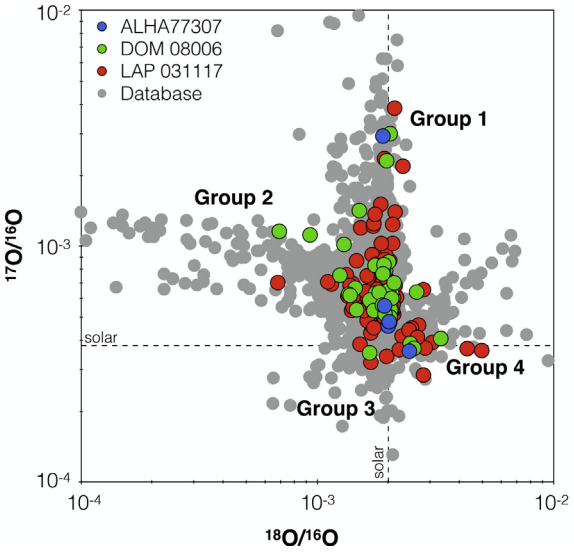

Fig. 2. Oxygen three-isotope plot ($^{17}O/^{16}O$ vs $^{18}O/^{16}O$) showing the O isotopic compositions of presolar silicate and oxide grains in LAP 031117 (131 grains), DOM 08006 (55 grains) and ALHA77307 (5 grains), compared with literature data from Bose et al. (2010a, 2012), Floss and Stadermann (2009b, 2012), Floss et al. (2008), Leitner et al. (2012, 2016b), Vollmer et al. (2009), Zhao et al. (2010, 2011, 2013) and the Presolar Grain Database (Hynes and Gyngard, 2009). The group classification is from Nittler et al. (1997).

like silicates are from AGB stars and 11% are from type II supernovae, while 95% of the olivine-like silicates are from AGB stars and 5% are from type II supernovae. The majority of presolar silicates have non-stoichiometric elemental compositions, not consistent with either pyroxene or olivine, including 8 Si-rich silicates ((Fe + Mg(+Ca))/Si < 1), 22 intermediate silicates ((Fe + Mg(+Ca))/Si between 1 and 2) and 46 Si-poor silicates ((Fe + Mg(+Ca))/Si > 2; Fig. 3). The overall distribution of compositions for presolar silicate grains from the CO3.0 chondrites is similar to those reported in other primitive carbonaceous chondrites (Fig. 3a; e.g., Vollmer et al., 2009; Floss and Stadermann, 2009b; Nguyen et al., 2010; Bose et al., 2012; Floss and Stadermann, 2009a). Presolar silicate grains in different matrix regions and FGRs in LAP 031117 and DOM 08006 do not show any significant differences in their average elemental compositions, and silicate grains exhibit a large range of Fe/Si and Mg/Si ratios (Fe/Si up to ~3.5 and Mg/Si up to ~3; Fig. 3b). The average Mg/Si and Fe/Si ratios (0.67 and 0.87, respectively) for all of the presolar silicate grains in the three meteorites are similar to GEMS (glass with embedded metal and sulfides) grains identified in IDPs (Keller and Messenger, 2011). Most (66%) of the 148 ferromagnesian silicate grains are Fe-rich (Fe/Mg ratios higher than 1.2), with iron contents up to 36 at.% (median = 17 at.%, Fig. 4). Apart from area 5 in LAP 031117, the median Fe contents in presolar silicates in CO3.0 chondrites are similar to those observed in primitive meteorites (Fig. 4). Thirteen of the presolar silicates also contain detectable amounts of Ca. In LAP 031117, presolar silicate grains in the matrix and FGRs have similar elemental compositions with median Fe contents of 17 ± 2 at.% and 20 ± 3 at.%, respectively. The median Fe content of presolar silicate grains in area 5 is about two times higher (~33 at.%) than other matrix areas (Fig. 4). TEM analysis of two presolar silicates in LAP 031117 (LAP-81 and LAP-104) confirmed that they are both silicate grains. Indeed, LAP-81 is crystalline with slightly different orientations on the left and right sides of the grain (the left side has a non-stoichiometric composition and the right side of the grain is a Ca-bearing olivine, Zega et al., 2014). LAP-104 is a complex grain composed of a fine-grained (10–70 nm) polycrystalline aggregate of Fe-Mg-Al-Ca silicate-bearing materials (Zega et al., 2014).

We also found 35 carbon-anomalous presolar grains: 27 in LAP 031117, two in ALHA77307 and six in DOM 08006. Thirty-one grains are ^{13}C-rich relative to solar ($^{12}C/^{13}C$ between 1.41 and 74). Auger analysis of grain LAP-149 indicated that it consists only of C, and a Raman spectroscopy measurement confirmed that it is a presolar graphite grain (Haenecour et al., 2016a). TEM analysis of grain LAP-31 showed that it is a SiC grain (3C-SiC polytype) with several TiC subgrains (Croat et al., 2015). The remaining ^{13}C-rich grains are probably SiC. The other four grains exhibit enrichments in ^{12}C ($^{12}C/^{13}C$ between 101 and 537) relative to solar. Auger analysis of one of these grains, LAP-141, indicated that it is only composed of C, suggesting that it is probably a graphite grain. The Auger distribution elemental maps also show the presence of a small iron sulfide subgrain inside grain LAP-141 (Haenecour et al., 2016a). We did not measure the elemental composition of the three other grains; they could be either SiC, graphite grains or some other C-rich phase.

3.2. Mineralogies and elemental compositions of distinct matrix areas and individual FGRs in LAP 031117 and ALHA77307

The EPMA measurements show that the matrix and FGRs in LAP 031117 and ALHA77307 have similar elemental compositions on a 10 μm-scale and are consistent with previous observations from Brearley (1993). The EPMA analyses of matrix areas and FGRs in LAP 031117 and ALHA77307 give totals that are low by ~11% (mean value = 11 ± 4%, Fig. 5). Three properties of fine-grained material are potentially responsible for low analytical totals: interstitial porosity within the fine-grained material, or the water and carbon contents (e.g., Trigo-Rodriguez et al., 2006). Because CO3 chondrites are known to have very low C (<1 wt.%; Greenwood and Franchi, 2004) and water contents (e.g., very limited occurrence of hydrous minerals), it is likely that the low totals mostly reflect porosity within the fine-grained material. This observation is also consistent with the average porosity measured in CO chondrites (10.8%; Consolmagno et al., 2008). As shown in Fig. 5, all individual matrix areas and FGRs in LAP 031117 and ALHA77307 have similar low totals (~11%), thus suggesting that they are all characterized by similar porosities.

As shown in Fig. 6, we identified a unique composite FGR (FGR 2) in ALHA77307, consisting of a small chondrule (~100 μm in diameter) surrounded by its own distinct

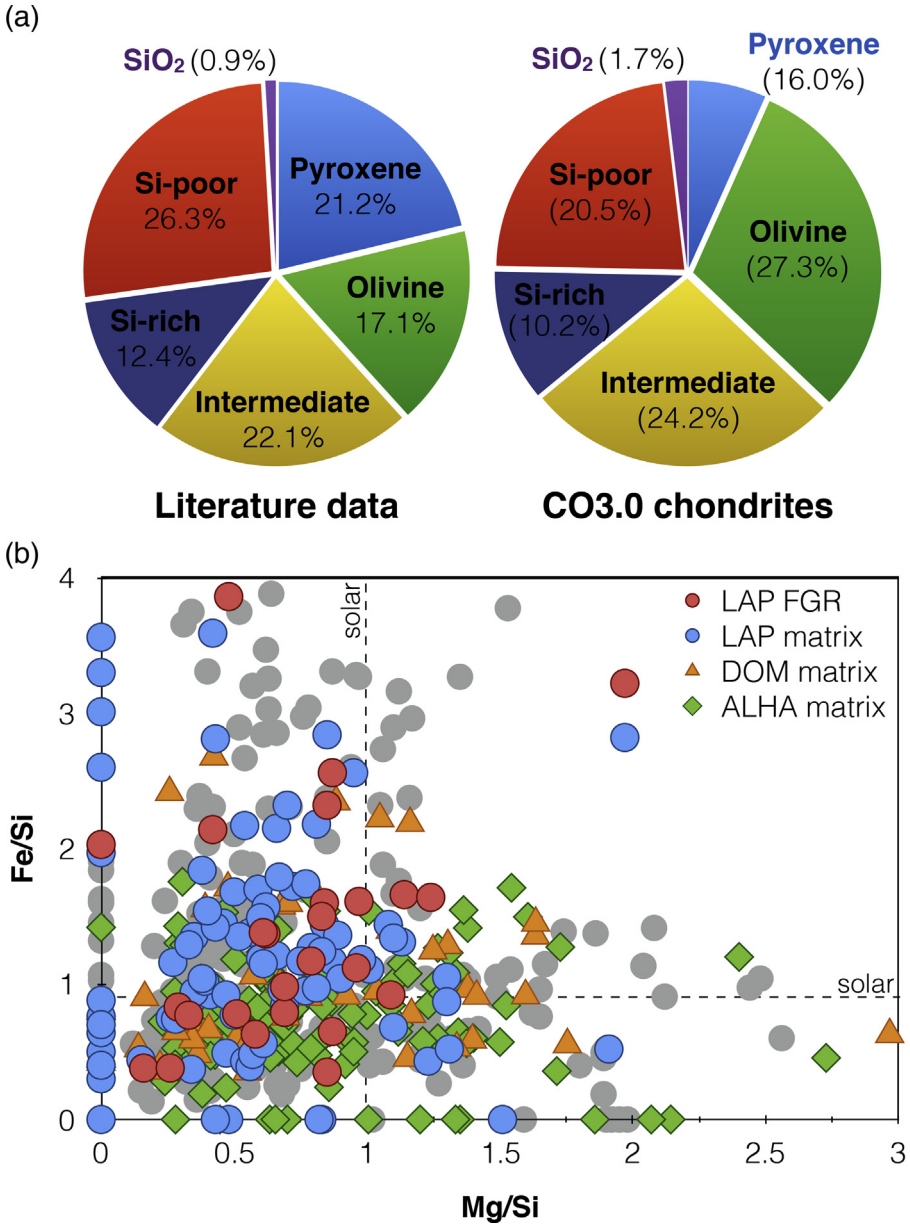

Fig. 3. (a) Classification of presolar silicate grains in ALHA77307, LAP 031117 and DOM 08006 based on their (Fe + Mg(+Ca))/Si ratios, compared with those in other chondrites. (Fe + Mg(+Ca))/Si ratio <1 (Si-rich), ~1 (pyroxene), between 1 and 2 (intermediate), ~2 (olivine) and >2 (Si-poor). (b) Auger elemental compositions (Mg/Si vs Fe/Si) of presolar silicate grains in LAP 031117 (matrix and fine-grained rims), DOM 08006 and ALHA77307. Grey circles are literature data. Data for LAP 031117 and DOM 08006 are from this study and data for ALHA77307 are from Bose et al. (2012) and Nguyen et al. (2010); literature data are from Bose et al. (2010a), Floss and Stadermann (2009a, 2012), Vollmer et al. (2009) and Zhao et al. (2013).

rim (FGR 3) within the FGR of a larger chondrule (~300 μm in diameter). Based on the law of included fragments in relative geologic dating, the smaller rimmed chondrule had to form before the larger one.

A TEM study of five FIB cross sections extracted from the LAP 031117 meteorite (four in the matrix and one in FGR1) indicates that the matrix is mainly composed of a mixture of amorphous material, nanocrystalline ferromagnesian silicates and anhydrous silicate grains (Fig. 7). Only minor signs of aqueous alteration (e.g., one isolated fibrous silicate) were identified in area 4; no phyllosilicates were identified in the other FIB sections. We also found evidence of sporadic terrestrial weathering in the FIB section of matrix area 5 with the identification of a large Fe-rich vein. Detailed study of the FIB section of FGR1 showed signs of extensive aqueous alteration with the presence of many sheet silicates, in particular smectite-like phyllosilicates (with a d-spacing of about 1 nm) mixed within a groundmass of fine fibrous silicates (Fig. 7).

We acquired Raman spectra in matrix areas of LAP 031117 and DOM 08006 to compare the degree of maturity of the organic matter and confirm their petrologic type.

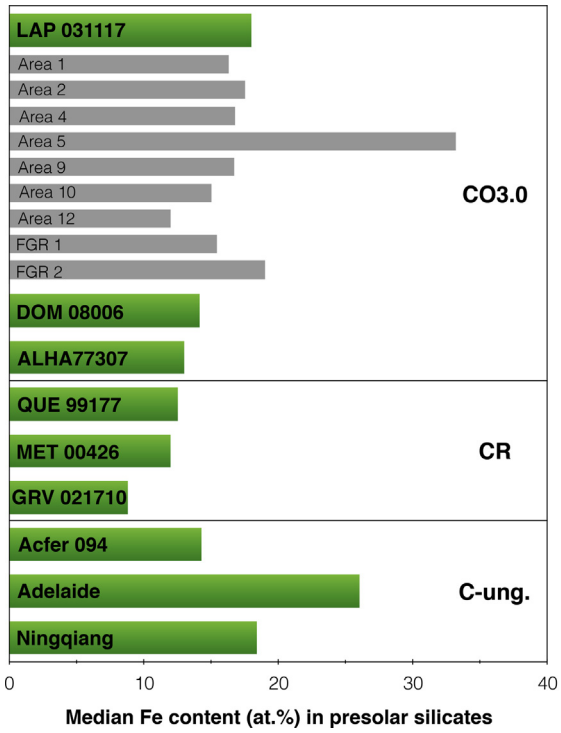

Fig. 4. Median Fe content (at.%) of presolar silicate grains in LAP 031117, DOM 08006 and ALHA77307 compared with other carbonaceous chondrites. Grey data correspond to individual matrix areas and FGRs in LAP 031117. Data for ALHA77307 are from Bose et al. (2012) and Nguyen et al. (2010); Data for other chondrites are from Floss and Stadermann (2009a,b, 2012), Vollmer et al. (2009) and Zhao et al. (2010, 2011, 2013).

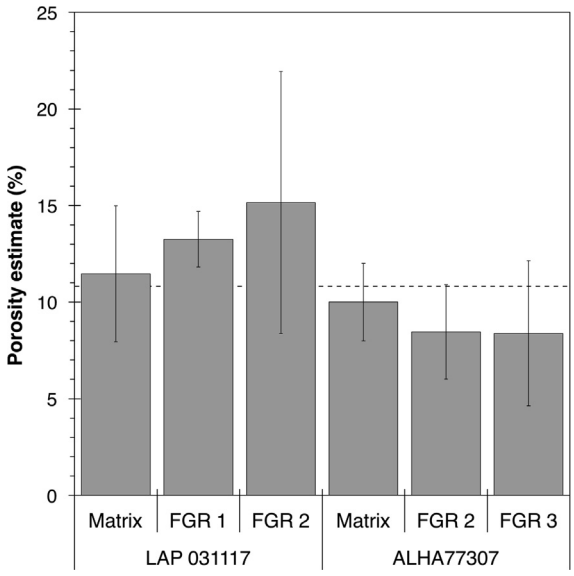

Fig. 5. Porosity estimates (%) based on EPMA measurements in LAP 031117 and ALHA77307. The dashed line corresponds to the porosity calculated for CO3.0 chondrites by Consolmagno et al. (2008).

Like the ALHA77307 meteorite (Bonal et al., 2006), the Raman spectra of LAP 031117 and DOM 08006 show both D- and G-band carbon features and have ratios of their peak height intensities (I_D/I_G) significantly lower than 1 ($I_D/I_G = \sim 0.8$; Fig. S1). These results are similar to new observations from Bonal et al. (2016) that showed that DOM 08006 and LAP 031117 have similar I_D/I_G ratios ($I_D/I_G = 0.8$), confirming that they are type 3.00–05 chondrites.

4. DISCUSSION

This study reports on the identification of presolar grains (silicates, oxides, SiC, and graphite) in the matrix and fine-grained chondrule rims from three CO3.0 chondrites, LAP 031117, DOM 08006 and ALHA77307. Below we compare the distribution of presolar grains between different fine-grained areas (matrix and FGRs) in these meteorites, and discuss what they tell us about the accretion and secondary processing of meteoritic fine-grained material in the solar nebula and on their parent body asteroids.

4.1. Isotopic compositions and stellar evolution of presolar grains in CO3.0 chondrites

As mentioned above, Nittler et al. (1997) defined four distinct groups of presolar oxide grains, based on their oxygen isotopic compositions. This classification reflects different origins, stellar processes, and/or properties of the parent stars. Previous studies of presolar silicate grains have shown that the distribution of their oxygen isotopic compositions is similar to that of the presolar oxides (Floss and Haenecour, 2016a). As in other meteorites, the majority of the presolar silicate-oxide grains in LAP 031117, ALHA77307 and DOM 08006 (~87%) belong to group 1 with enrichments in ^{17}O relative to solar, and subsolar to solar $^{18}O/^{16}O$ ratios (Fig. 2). We did not identify any 'extreme Group 1' grains (with $^{17}O/^{16}O > 6 \times 10^{-3}$; Gyngard et al., 2011). Group 1 grains are believed to originate from the envelopes of low- to intermediate-mass (1.2–2.2 $M_\odot$) thermally pulsing Red Giant Branch (RGB), or Asymptotic Giant Branch (AGB) stars of close-to-solar metallicity (Fig. 2; Nittler et al., 2008; Nittler, 2009). Five grains belong to Group 2 (solar $< ^{17}O/^{16}O < 4 \times 10^{-3}$ and $^{18}O/^{16}O < 1 \times 10^{-3}$) and are explained by condensation in low-mass red giant or AGB stars (less than 2 $M_\odot$) that experienced an extra deep mixing mechanism, called cool-bottom processing, which transfers material from the bottom of the envelope close to the hydrogen-burning shell and brings it back into the envelope (e.g., Wasserburg et al., 1995; Nollett et al., 2003), while destroying some of the ^{18}O in the process. However, new model calculations by Lugaro et al. (2017) showed that the O isotopic composition of Group 2 grains can also be explained by condensation in intermediate mass (4–8 $M_\odot$) AGB stars. Nineteen O-anomalous grains exhibit ^{18}O excesses characteristic of Group 4 grains (Fig. 2), and represent about 10% of all O-anomalous grains. Group 4 grains are believed to have condensed in the ejecta of core-collapse (Type II) supernovae, as their isotopic compositions are consistent with mixing of material from different layers of supernovae

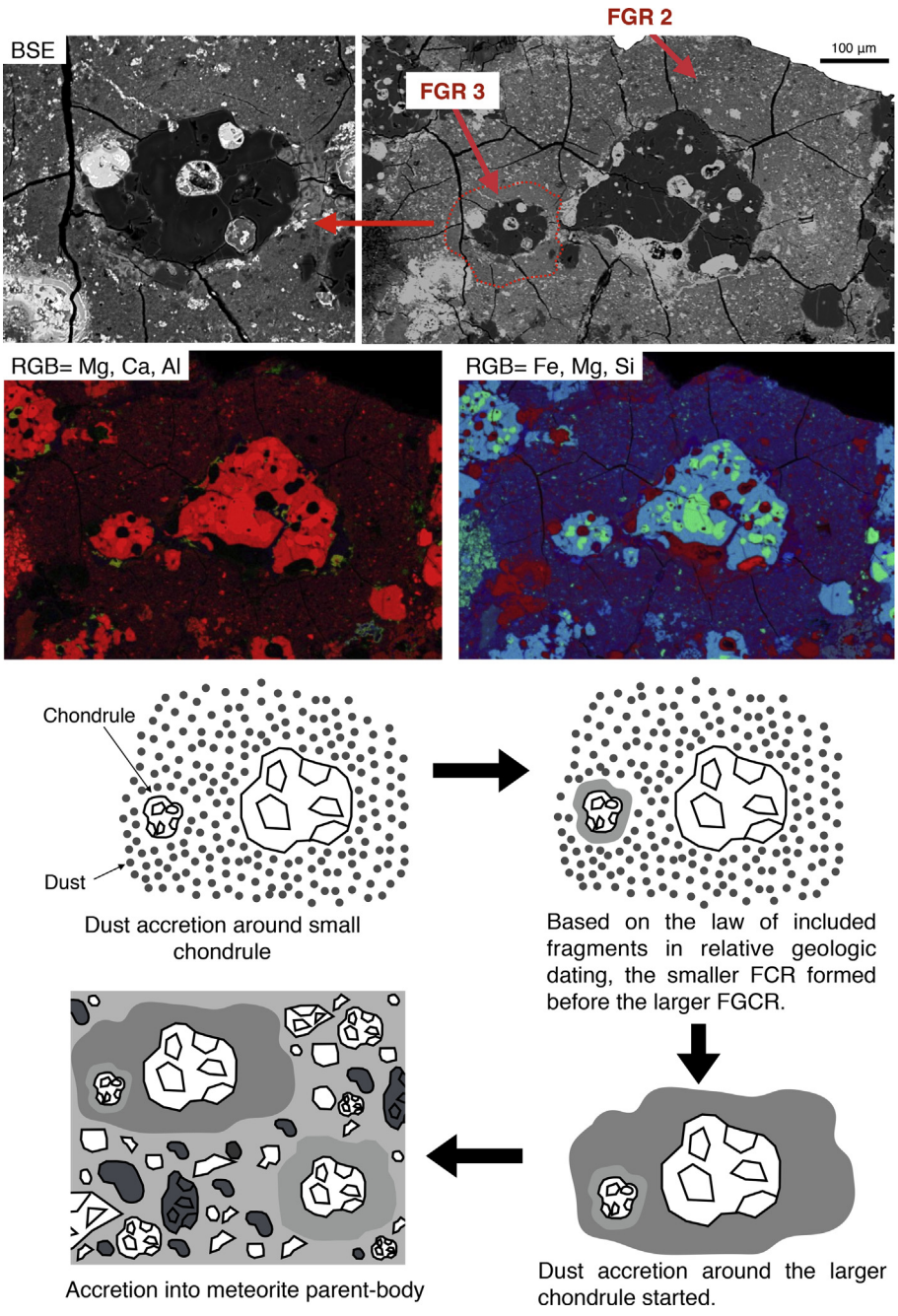

Fig. 6. Model scenario for the formation of a small-rimmed chondrule within a larger fine-grained chondrule's rim ('composite FGR'). The four upper panels show back-scattered electron (BSE) images and RGB X-rays elemental maps of the composite fine-grained chondrule rim in ALHA77307.

(Choi et al., 1998; Nittler et al., 2008). Finally, three grains belong to Group 3 with depletions in both ^{17}O and ^{18}O (Fig. 2). Their origins are not well-understood, but they may come from AGB stars with lower than solar metallicity or Type II supernovae, like the Group 4 grains.

Based on the presolar silicate grains identified in ALHA77307, Bose et al. (2012) suggested that there might be a difference in the compositions of presolar silicates from AGB stars and supernovae, with a higher olivine to pyroxene ratio for supernovae than for AGB stars. Combining the 190 O-anomalous grains in this study with previously reported O-anomalous grains in other carbonaceous chondrites (>500 grains), we can revisit this question by comparing the compositions and distributions of presolar silicate and oxide grains from low-mass AGB stars (Groups 1 and 2) and type II supernovae (Group 4). First, presolar silicate grains from AGB stars and supernovae have similar grain size distribution, with median sizes of about 275 nm. The proportions of silicate and oxide grains are also very similar, with silicate-to-oxide ratios of 12 ± 1

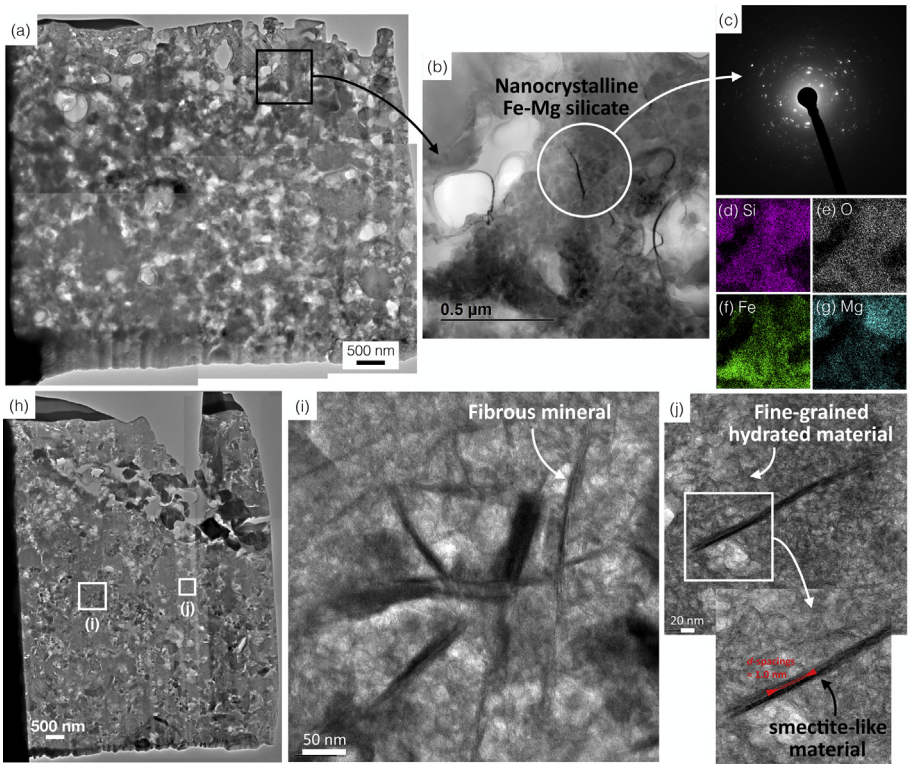

Fig. 7. TEM analysis of a matrix region (area 1) and FGR 1 in LAP 031117. (a) Bright-field scanning TEM (STEM) overview image of FIB-sections in matrix area 1. (b) is BF-STEM image of area outlined by rectangle in (a). (c) Selected area electron diffraction (SAED) pattern from area outlined by white circle in (b) showing that it is composed of amorphous and nanocrystalline material, without any fibrous minerals. (d–g) EDS elemental maps of the area shown in (b). (h) overview BF-STEM image of the FIB section in FGR 1. (i) BF-STEM image of area outlined by left rectangle in (h), showing the presence of fibrous minerals mixed within a groundmass composed of fine-grained fibrous material. (j) BF-STEM image of area outlined by left rectangle in (h), showing that the phyllosilicates in FGR 1 have d-spacings of about 1.0 nm.

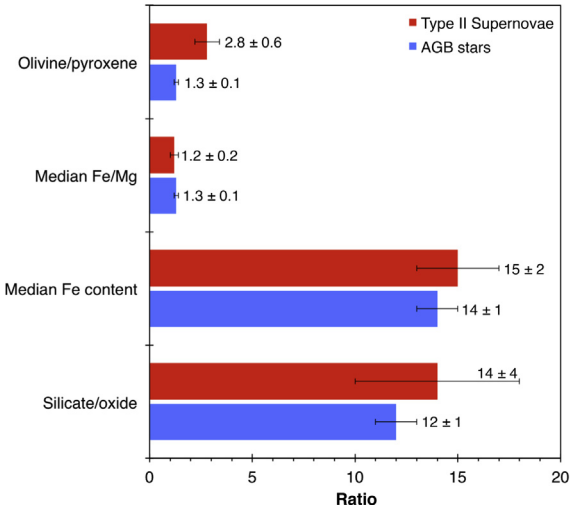

Fig. 8. Comparison of the elemental compositions, olivine/pyroxene ratios and silicate/oxide ratios of presolar silicate-oxide grains from AGB stars (groups 1–2) and type II supernovae (group 4). The calculations include the data from this study and all other Auger data available for presolar silicate and oxide grains: Bose et al. (2010a, 2010b, 2012), Floss and Stadermann (2009b, 2012), Floss et al. (2008), Nguyen et al. (2010), Vollmer et al. (2009), Zhao et al. (2011, 2013).

and 14 ± 4, respectively (Fig. 8); this ratio is significantly lower than a theoretical estimate of ~23 for the dust from AGB stars (Leitner et al., 2012). As shown in Fig. 8, the compositions of ferromagnesian presolar silicate grains from AGB stars and supernovae are also virtually identical, with median Fe contents of ~15 at.% and median Fe/Mg ratios of ~1.3. However, the distribution of different types of presolar silicates (olivine vs. pyroxene) is significantly different between AGB stars and type II supernovae, with olivine-to-pyroxene ratios of 1.3 ± 0.1 and 2.8 ± 0.6, respectively. This difference is consistent with the initial observation by Bose et al. (2012), and indicates that pyroxene and olivine grains from AGB stars were included in similar proportions in the solar nebula, while more olivine than pyroxene grains from supernova were incorporated. The reason for this difference is still unclear, and could reflect either the original distribution of presolar grains (more olivine than pyroxene grains condense in supernovae), the preferential alteration/destruction of olivine grains from AGB stars, or the preferential alteration/destruction of pyroxene grains in SNe. However, it is important to note that, while the proportions of olivine and pyroxene grains are different in AGB stars and supernovae, most presolar silicates (~60%) have nonstoichiomet-

ric compositions, inconsistent with either pyroxene or olivine.

Of the 35 C-anomalous presolar grains identified in LAP 031117, ALHA77307 and DOM 08006, 31 grains are ^{13}C-rich relative to solar (^{12}C/^{13}C between 1.41 and 74). Haenecour et al. (2016a) showed that grain LAP-149 is a graphite grain and has C, N, Si, S isotopic compositions that are consistent with condensation in the ejecta of a low-mass CO nova. While we do not have Auger measurements for all of the other ^{13}C-rich grains, most are likely SiC grains and their carbon isotopic ratios are consistent with mainstream grains (^{12}C/^{13}C ratios between 10–100); however, this classification cannot be confirmed without knowing their Si and/or N isotopic compositions. Mainstream SiC grains are thought to originate from low-mass (1–3 $M_{\odot}$) carbon stars, a class of AGB stars in which the stellar envelope has C/O > 1, a necessary condition for the condensation of C-rich grains (Zinner, 2014). The other four grains exhibit enrichments in ^{12}C (^{12}C/^{13}C between 101 and 537) relative to solar. Auger analysis of one of these grains, LAP-141, showed that it is only composed of carbon and is thus likely a graphite grain (Haenecour et al., 2016a). The three other ^{12}C-rich grains could either be SiC, graphite or some type of disordered carbonaceous matter (e.g., Floss and Stadermann, 2009b).

4.2. Overall presolar grain abundances: uniform initial distribution of presolar grains in CO3 chondrites

The presolar grain abundances are determined from the ratio of area of the presolar grains to the total area analyzed (expressed in parts per million, or ppm). The abundances are not corrected for detection efficiency and the errors are calculated from the respective standard deviations of the grain numbers based on Poisson statistics. For abundances based on a small number of grains (less than 10), asymmetric errors were calculated from confidence limits for small numbers (Gehrels, 1986). All errors on the abundances reported in this study are 1σ, unless stated otherwise. The O-anomalous grains consist of both silicates and oxides, and the C-anomalous grains comprise both SiC and graphite grains. However, given the low abundance of presolar oxide and graphite grains (≤12 ppm, Table 1) in CO3 chondrites, the abundances of O-anomalous and C-anomalous grains are largely dominated by the presolar silicate and SiC grains, respectively.

Based on all the presolar grains identified in this study and by Bose et al. (2012) and Nguyen et al. (2010), we calculate an overall presolar O-anomalous grain abundance in CO3.0 chondrites of 165 ± 9 ppm (Fig. 9). Based on our data, all three CO3.0 chondrites have overall O-anomalous grain abundances that are the same within errors: 150 ± 13 ppm for LAP 031117, 162 ± 16 ppm for ALHA77307, and 160 ± 22 ppm for DOM 08006 (Table 1, Fig. 9). Table 1 also provides the detailed presolar grain abundances in the matrix and FGRs in the three meteorites. Our estimate of the presolar O-anomalous grain abundance in DOM 08006 is significantly lower than the abundance (240 ± 25 ppm) reported by Nittler et al. (2013). However, if we consider the O-anomalous grain abundance only in the matrix of DOM 08006, then our estimate (227 ± 32 ppm, Table 1) is in agreement with Nittler et al. (2013) within 2σ errors. Recently, Haenecour and Floss (2016) reported a low abundance of presolar silicate grains (44 ± 13 ppm) in the CO3.0 chondrite Northwest Africa 8631 (NWA 8631), suggesting that, despite its initial classification, it is likely not a type 3.0 CO chondrite but is of higher petrologic type, possibly 3.1–2.

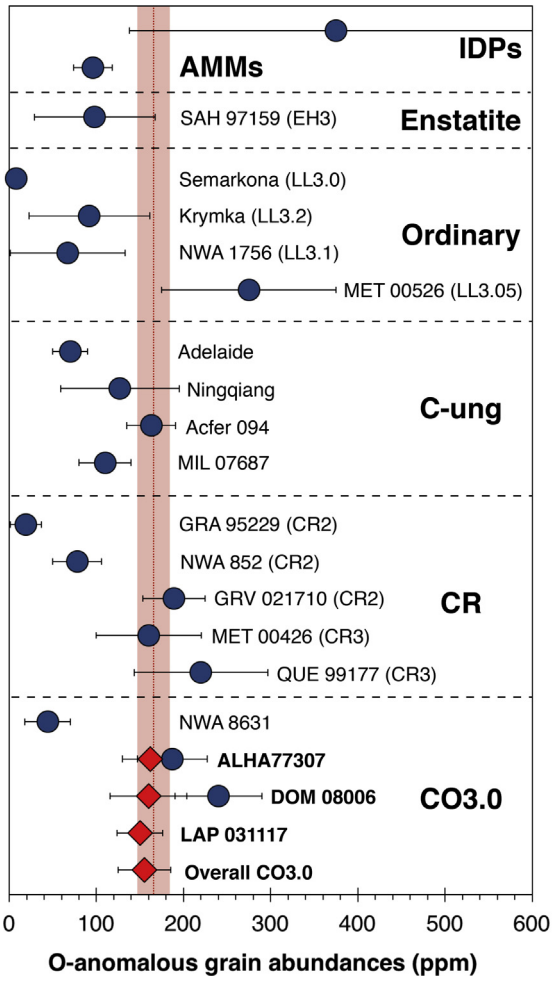

Fig. 9. Abundances of O-anomalous grains (silicates and oxides) in the CO3.0 chondrites ALHA77307, LAP 031117 and DOM 08006 compared with other ordinary and carbonaceous chondrites, micrometeorites (AMMs) and IDPs. Errors are 2σ. Red diamonds are abundances based on data from this study, and blue circles are from literature data (Bose et al., 2010b, 2012; Floss and Haenecour, 2016b; Floss and Stadermann, 2009a; Floss and Stadermann, 2012; Haenecour and Floss, 2016; Leitner et al., 2012, 2014, 2016b; Nguyen et al., 2010; Nittler et al., 2013; Vollmer et al., 2009; Zhao et al., 2010, 2011, 2013. The shaded area corresponds to the overall O-anomalous grain abundance in CO3.0 chondrites (including all data in this study, Bose et al. (2012) and Nguyen et al. (2010)). (For interpretation of the references to colour in this figure legend, the reader is referred to the web version of this article.)

Comparison of the abundances of presolar silicate grains in IDPs, micrometeorites, and different groups of meteorites (Fig. 9) shows that there are large variations in the presolar grain abundances among different extraterres-

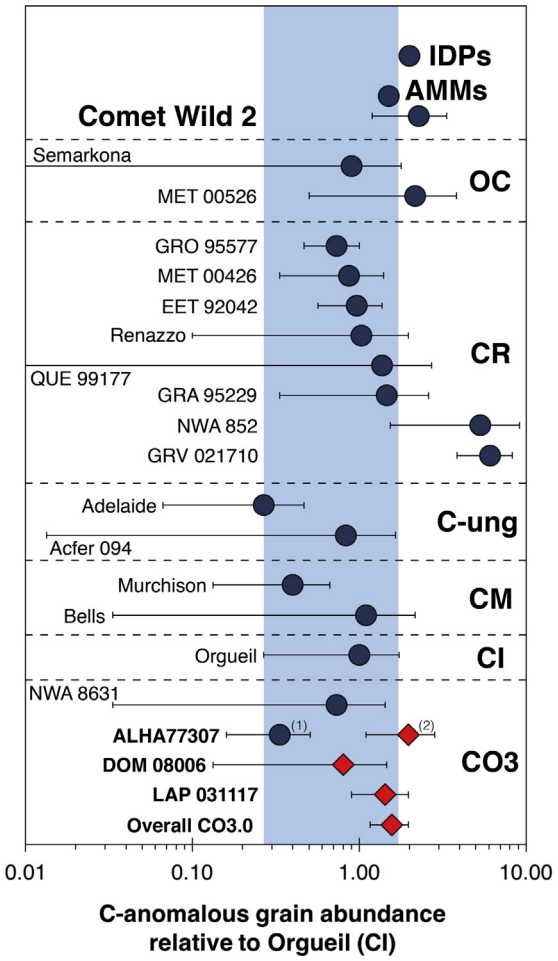

Fig. 10. Matrix-normalized C-anomalous grain abundances in CO3.0 chondrites and other ordinary and carbonaceous chondrites relative to the Orgueil meteorite (CI). Red diamonds are abundances based on data from this study, and blue circles are from literature data (Davidson et al., 2014a and references therein; Floss and Stadermann, 2009b, 2012; Leitner et al., 2012; Zhao et al., 2013). The blue shaded area corresponds to the abundance in the CI chondrite Orgueil. (1) abundance from Davidson et al. (2014a), (2) abundance calculated from data in this study and Bose et al. (2012). Errors are 2σ. (For interpretation of the references to colour in this figure legend, the reader is referred to the web version of this article.)

trial materials and that only a handful of the most primitive meteorites contain high abundances of presolar silicates. The overall abundances of O-anomalous grains in the three CO3.0 chondrites are comparable to abundances determined for other primitive carbonaceous chondrites (e.g., QUE 99177 and Acfer 094; Fig. 9).

Combining all 65 carbon-anomalous grains identified in this study and by Bose et al. (2012), we estimated an overall C-anomalous grain abundance of 47 ± 6 ppm for CO3.0 chondrites (43 ± 8 ppm for LAP 031117, 59 ± 13 ppm for ALHA77307 and 24^{+15}_{-10} ppm for DOM 08006; Table 1 and Fig. 10). As mentioned above, two C-anomalous grains identified in LAP 031117 are presolar graphite grains, representing the first presolar graphites identified *in-situ*, and corresponding to an abundance of 5^{+7}_{-3} ppm (Haenecour et al., 2016a). As shown in Fig. 10, the abundances of presolar SiC grains in the three CO3.0 chondrites are consistent with those in other carbonaceous and ordinary chondrites, and, apart from GRV 021710 (Zhao et al., 2013), all meteorites, IDPs and micrometeorites have abundances similar to the CI chondrite Orgueil, within 2σ errors. This observation is consistent with the proposition by Alexander (2005) that the presolar grains in the matrix of all chondrite groups accreted from a common reservoir. As previously suggested by Davidson et al. (2014a), Fig. 10 also shows that there is no variation of the presolar SiC grain abundances with the degree of aqueous alteration experienced by each meteorite (e.g., CR chondrites). However, other studies (Huss and Lewis, 1995; Huss et al., 1996, 2003, 2006) of more thermally altered meteorites have demonstrated that the presolar SiC grain abundances within each chondrite class correlate with their respective degree of thermal metamorphism.

In summary, the fact that both the overall O-anomalous (~155 ppm) and C-anomalous grain abundances (~40 ppm) are the same within errors in all three CO3.0 chondrites provides evidence that they likely accreted from a nebular reservoir with similar presolar grain abundances.

4.3. Presolar grain abundances in individual fine-grained areas: evidence for a nebular origin of FGRs in CO3 chondrites

4.3.1. Identification of presolar grains in fine-grained rims of CO3.0 chondrites

We searched for presolar grains in two distinct FGRs from LAP 031117, one from DOM 08006 and two from ALHA77307 (including one from Bose et al., 2012), and identified presolar grains, including both O-anomalous (silicates and oxides) and C-anomalous grains in all five FGRs. Apart from FGR 2 in ALHA77307, the presolar O-anomalous and C-anomalous grain abundances are similar in all FGRs with overall abundances of 67 ± 10 ppm and 53 ± 13 ppm, respectively.

The identification of presolar grains in FGRs definitively excludes direct formation of the rims from adjacent chondrule material, but is consistent with a nebular origin for the rims, as also concluded by Leitner et al. (2016a,b) for CR chondrites. Formation on the parent body asteroid by impact-related compression cannot be excluded based only on the presence of presolar grains in the rims. However, model calculations (Bland et al., 2012, 2014; Dyl et al., 2012) show that low-pressure (<4–5 GPa) impacts on parent-body asteroids induce large temperature increases limited to the fine-grained material around chondrules that can equilibrate the oxygen isotopic composition of presolar silicate grains on short timescales. Thus, the presence of abundant presolar silicate grains in the FGRs argues against this model.

4.3.2. Presolar grain abundances in individual fine-grained areas: systematically lower abundances of presolar silicate-oxide grains in fine-grained chondrule rims of CO3 chondrites

Large variations in the presolar grain abundances (up to 120 ppm) between different individual matrix areas have

been previously observed within other meteorites (e.g., Zhao et al., 2011). Assuming that all CO3 chondrites indeed accreted from nebular reservoir(s) with similar presolar grain abundances, the variations in presolar grain abundances observed from one meteorite to another (e.g., between NWA 8631 and DOM 08006, Fig. 9) or between different fine-grained areas in the same meteorite reflect the alteration history of the host meteorite or its individual components, such as FGRs (e.g., Floss and Haenecour, 2016a). Because presolar silicates are more susceptible to heating and aqueous alteration than the other more refractory presolar phases (e.g., SiC), comparison of the presolar silicate abundances in various meteorites can constitute a proxy to evaluate the degree of "primitiveness" of these meteorites (Floss and Stadermann, 2012; Floss and Haenecour, 2016a). Terrestrial aqueous alteration may also be responsible for the destruction or re-equilibration of the isotopic composition of some presolar silicates. However, Leitner et al. (2012) have shown that terrestrial weathering does not seem to have a significant influence on the overall presolar silicate abundances in CR chondrites. Moreover, the three CO3.0 chondrites in this study only show very limited and localized signs of terrestrial alteration.

To investigate the homogeneity of the presolar grain abundances within the CO3.0 chondrites and identify any possible significant variations from one fine-grained area to another, we searched for presolar grains in both individual matrix areas and fine-grained chondrule rims from the LAP 031117 and DOM 08006 meteorites, as well as in a FGR from ALHA77307 (FGR1). We tried to search large total areas (in general more than 5000 μm^2) in each region to be able to observe any statistically relevant variations. We excluded all the data of one region of LAP 031117, area 8, from the matrix abundance calculations, as this area could in fact be a broken FGR (on the border of the thin section, Fig. 1). In addition to comparing the presolar grain abundances in individual matrix areas, we also calculated the grain number densities (number of grains per 100 square micrometers) in order to evaluate whether the abundance estimates were affected by biases, such as the presence of a significantly larger than usual presolar grain, as grain number densities have the advantage of being independent of grain size (Floss and Brearley, 2014). However, as shown in Fig. 11, the O-anomalous grain abundances and number densities of the matrix areas and FGRs are highly correlated ($R^2 = 0.9$), indicating that the abundances were not affected by any grain size bias.

As shown in Fig. 12a, apart from FGR 2 in ALHA77307, comparison of the presolar silicate abundances in the interstitial matrix regions and individual FGRs in CO3.0 chondrites (LAP 031117, ALHA77307, DOM 08006) shows systematically lower abundances of O-anomalous grains in the FGRs than in the different individual matrix areas with average abundances of 186 $\pm$ 13 ppm and 67 $\pm$ 10 ppm, for the matrix and FGRs respectively (Fig. 12a). Davidson et al. (2012) also reported a lower presolar silicate abundance in an individual FGR than in the matrix of ALHA77307. In contrast to the O-anomalous abundances, the abundances of C-anomalous grains in the FGRs and matrix regions of LAP 031117,

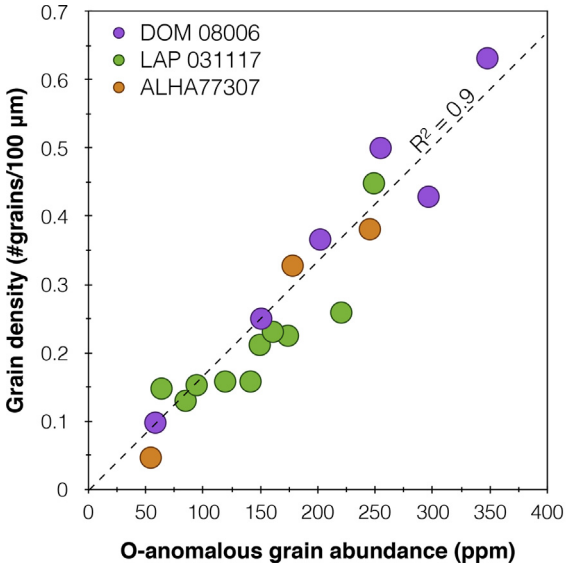

Fig. 11. Comparison of abundances (parts-per-million) and number density (number of grains/100 μm^2) of O-anomalous grains in different fine-grained areas from ALHA77307, DOM 08006 and LAP 031117. Data for ALHA77307 are based on presolar grains from this study and Bose et al. (2012).

ALHA77307 and DOM 08006 are the same within 1σ errors (Fig. 12b). SiC grains are more resistant to secondary processing (e.g., thermal metamorphism and aqueous alteration) than silicate grains (e.g., Floss and Stadermann, 2012; Leitner et al., 2012), suggesting that the systematic difference in O-anomalous grain abundances observed between the matrices and FGRs in these three meteorites reflects some type of preferential destruction of presolar silicates by secondary processing in the FGRs without affecting the matrix. This secondary processing of the FGR could have happened either in the solar nebula before the incorporation of chondrules into planetesimals ("pre-accretionary alteration"), or on the parent body asteroid.

Only one matrix region in LAP 031117, area 5, has an O-anomalous grain abundance between the average abundances of the matrix and FGRs within 1σ errors (Fig. 12a). The lower abundance of presolar silicates in this area might reflect destruction of some presolar silicates by limited and localized terrestrial weathering, as this region is crossed by a large Fe-rich vein. Chizmadia and Cabret-Lebron (2009) also report the presence of sporadic Fe-rich terrestrial alteration veins in LAP 031117. The presolar silicate grains in area 5 also exhibit significantly higher Fe contents (median Fe content = 33 at.%, Fig. 4), and TEM analysis indicates a higher proportion of magnetite grains in this area. These observations provide evidence that presolar silicates in this area were affected by alteration, possibly terrestrial weathering in the Antarctic ice.

To further constrain the cause of the systematic difference in presolar silicate abundances between FGRs and matrix regions in CO3.0 chondrites, we compared the bulk elemental compositions of LAP 031117 and ALHA77307, and the mineralogy and elemental compositions of presolar silicates in several FGRs and matrix regions in LAP

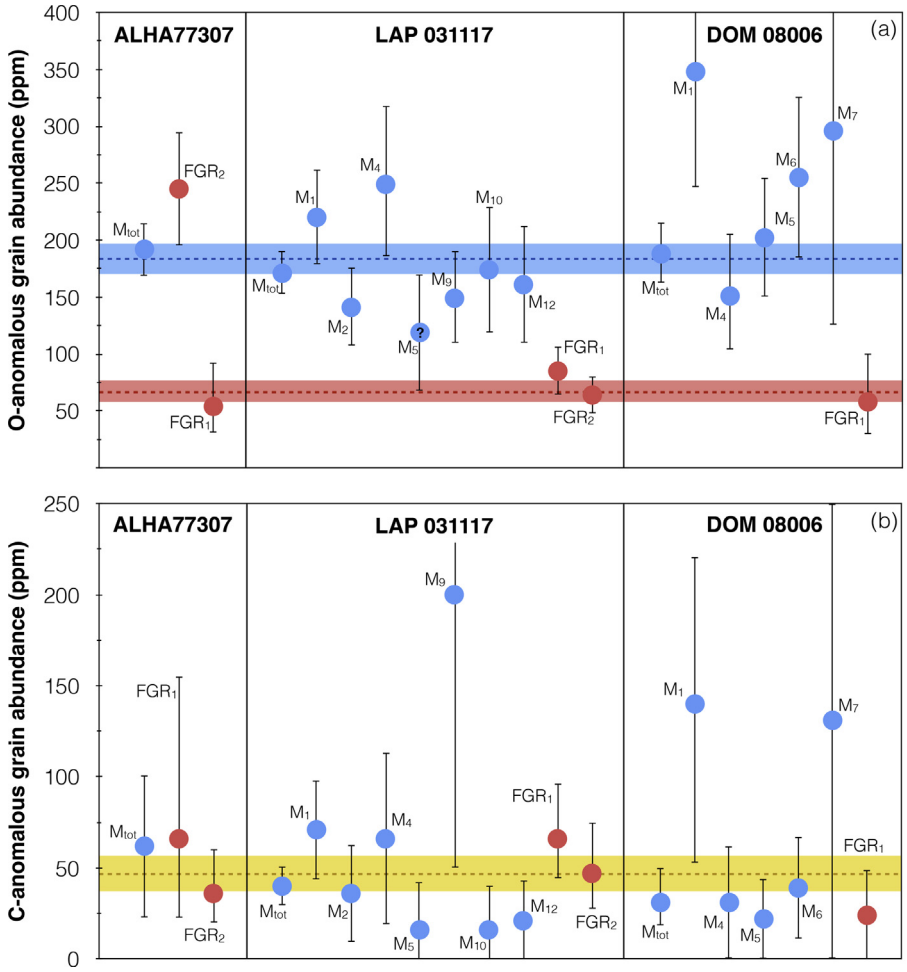

Fig. 12. Comparison of (a) O-anomalous and (b) C-anomalous grain abundances in individual matrix areas (blue dots) and FGRs (red dots) in LAP 031117, DOM 08006 and ALHA77307. The blue and red shaded areas correspond to the average O-anomalous grain abundances in all matrix and FGRs, respectively. The yellow shaded area corresponds to the overall abundance of C-anomalous grains in all three meteorites. Errors are 1σ. (For interpretation of the references to colour in this figure legend, the reader is referred to the web version of this article.)

031117. The EPMA measurements show that matrix regions and FGRs in LAP 031117 and ALHA77307 have very similar bulk elemental compositions on a 10 μm-scale. This observation is consistent with previous observations of the ALHA77307 meteorite by Brearley (1993). The elemental compositions of presolar grains between different matrix regions (excluding area 5) and FGRs in LAP 031117 exhibit large, but similar, ranges of Fe/Si and Mg/Si ratios (Fig. 3). Moreover, the median Fe contents of presolar ferromagnesian silicates are the same in the matrix and FGRs (~15 at.%, Fig. 4). These observations are also consistent with recent measurements of the elemental compositions of >1000 submicron non-presolar silicate grains, which show no significant compositional differences between individual matrix regions and FGRs in LAP 031117 (Haenecour et al., 2016b). In summary, the variations in O-anomalous grain abundances between the matrix and FGRs in LAP 031117 do not correlate with any significant variations in either the bulk elemental composition, or the elemental compositions of submicron presolar and non-presolar silicate grains in each of these areas.

Recent numerical simulations of impact-related compaction in chondritic meteorites (Bland et al., 2012, 2014; Dyl et al., 2012) suggest that the systematically lower abundances of O-anomalous grains in the FGRs could reflect the destruction or equilibration of the oxygen isotopic composition of some presolar silicate grains in the FGRs by low-pressure (<4–5 GPa) impacts. Bland et al. (2014) proposed that low-intensity impacts might have played an important role in the compaction of carbonaceous chondrites; in particular, their model suggested that these impacts might have a significant effect on the fine-grained material around chondrules as a result of large temperature increases (<1450 K) that are limited to the material surrounding chondrules. Dyl et al. (2012) calculated the oxygen isotope diffusion in submicron presolar silicate grains during low-pressure shock events and showed that such temperature increases were capable of homogenizing the oxygen isotopic composition of submicron (250–500 nm) presolar silicate grains on timescales of 1–10 s. However, their model also suggests that these impacts would increase Fe-Mg diffusion in submicron silicate grains (e.g. olivine grains) leading to a

significant decrease in the average Fe content of these grains (Dyl et al., 2012), which we do not observe in our data. Moreover, their model requires high water and oxygen fugacity conditions (by the potential fluid volatilization accompanying the low-pressure shocks) to homogenize the isotopic composition of presolar silicates on a reasonable timescale, but CO3.0 chondrites do not have high water contents (e.g., Jarosewich, 1990) and evidence for their alteration appears to be very localized (e.g., Brearley, 1993).

We also carried out detailed TEM analysis of matrix areas 1, 4 and 10, and FGR 1 in LAP 031117. The three matrix areas are mainly composed of anhydrous Fe-Mg silicate grains in a groundmass of amorphous silicates and nanocrystalline material (Fig. 7), and, apart from the identification of a few isolated fibrous silicates in area 4, they do not exhibit significant signs of aqueous alteration. Brearley (1993) reported similar local occurrences of isolated phyllosilicates (d-spacing ~1 nm) in some matrix regions of ALHA77307. In contrast, FGR 1 shows evidence of extensive aqueous alteration with the identification of phyllosilicates (d-spacing = 1.0 nm, consistent with smectite-like material) mixed with a fine-grained fibrous groundmass throughout the FIB section (Fig. 7). Similar aqueous alteration was also reported in a FGR from the NWA 5717 ordinary chondrite (type 3.05), without any evidence for alteration in the matrix (Bigolski et al., 2013). The TEM observations are consistent with the presolar silicate abundances, with the more pristine interstitial matrix regions characterized by a significantly higher abundance (≥150 ppm) of O-anomalous grains than the aqueously altered fine-grained chondrule rim (~80 ppm). These observations suggest that localized (μm-scale) aqueous alteration in the FGRs is responsible for the destruction or re-equilibration of the oxygen isotopic compositions of some presolar silicates in the rims (without affecting the matrix regions), accounting for the spatial variation of presolar silicate abundances between the matrix and FGRs in CO3.0 chondrites. Such localized (μm-scale) aqueous alteration of the FGRs could have occurred either on the meteorite parent body by heterogeneities in water/ice circulation (e.g., Le Guillou and Brearley, 2014), by aqueous alteration on precursor planetesimals (e.g., Metzler et al., 1992; Bischoff, 1998), or by ice melting in the solar nebula before the accretion of the chondrules and rims into asteroids (e.g., Bischoff, 1998; Ciesla et al., 2003).

4.4. Presolar grain abundances in fine-grained rims: comparison between CO3 and CR chondrites

The difference between the O-anomalous grain abundances in FGRs and matrix regions in CO3.0 chondrites is the opposite of observations in CR2 chondrites (Leitner et al., 2016b), where the combined overall O-anomalous grain abundances for five CR2 chondrites seem to be lower for interstitial matrix (~23 ppm) than for FGRs (~72 ppm; Fig. 13). However, with the exception of EET 92161 (Leitner et al., 2016a), the abundances overlap in individual CR2 chondrites, within 2σ errors, and it is important to also note that some of these abundances in FGRs combine data for several FGRs. Leitner et al. (2016b) also reported that the presolar grain abundances in the matrix and a FGR of the CR3 chondrite MET 00426 exhibit a similar trend as the CO3.0 chondrites. This suggests a difference between carbonaceous chondrites of petrologic type 3 (most pristine) and type 2 (aqueously altered). Presolar grain abundances in the matrix areas of both types of meteorites differ significantly, with much lower abundances in the matrix regions of type 2 chondrites than in the matrix regions of type 3 chondrites (Fig. 13). However, (with the exception of FGR 2 in ALHA77307) the fine-grained chondrule rims in both petrologic type 3 and 2 meteorites have similar O-anomalous grain abundances (~60–80 ppm), within errors (Fig. 13a). This observation thus suggests that the systematic higher overall O-anomalous grain abundances observed in type 3 (CO3 and CR3) compared to the one in type 2 (CR2) chondrites are due to lower

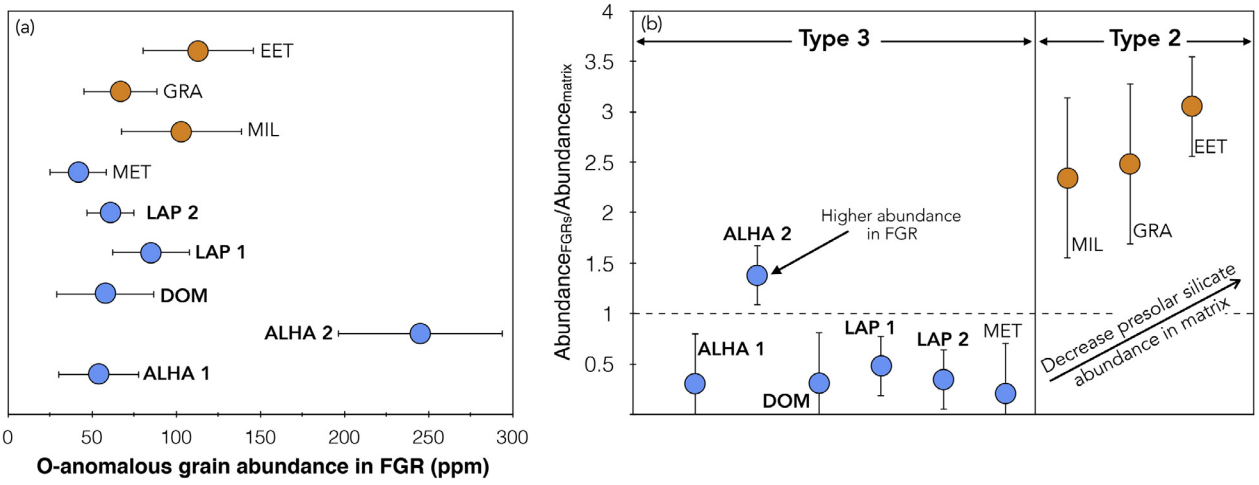

Fig. 13. (a) O-anomalous grain abundances in individual FGRs of petrologic type 3.0 CO (LAP 031117, DOM 08006, ALHA77307) and CR chondrites (MET 00426), and type 2 CR chondrites (EET 92161, MIL 07525, GRA 95229). (b) Ratio of the O-anomalous grain in individual FGRs and in the matrix of the same meteorites. Data for CO3 chondrites are from this study and CR chondrites from Leitner et al. (2016b). The number 1 and 2 next to LAP and ALHA refer to different fine-grained rims (FGR 1 and FGR 2) in each meteorite. Errors are 1σ.

O-anomalous grain abundances in the matrix of type 2 chondrites (Fig. 13b). The presolar SiC abundances are also similar within errors (~30–40 ppm) in all of the chondrites reported in Fig. 13 (Davidson et al., 2014a; Leitner et al., 2016a,b).

Aqueous alteration on the CR chondrite parent body is believed to be responsible for the lower abundance of presolar silicates in the matrix of CR2 chondrites than in CR3 chondrites (Floss and Stadermann, 2009a; Leitner et al., 2012, 2015), and Leitner et al. (2016b) suggested that the FGRs were less affected by the parent body aqueous alteration than the matrix because of their compacted nature. If this is the case, the difference in O-anomalous grains abundances observed between the matrix and FGRs in the type 3 chondrites (CO and CR) must reflect other, non-parent body secondary process(es). One possibility is that the low abundance of presolar silicate grains in the FGRs of both CO3 and CR chondrites is due to aqueous alteration in the solar nebula before dust and chondrule accretion into asteroids. Previous studies (e.g., Metzler et al., 1992; Lauretta et al., 2000) have proposed that the texture and mineralogical assemblages in FGRs of CM chondrites reflect their formation in the solar nebula from a mixture of altered (hydrous) and unaltered (anhydrous) dust grains before asteroid accretion. These models thus suggested that some materials in the FGRs were affected by pre-accretionary aqueous alteration in the solar nebula. The formation of hydrous minerals in the solar nebula has been discussed for decades. While phyllosilicates are thought to be thermodynamically stable under solar nebula conditions, Fegley and Prinn (1989) suggested that their formation via gas–solid reactions in the solar nebula would be kinetically inhibited. However, other studies have proposed that phyllosilicates could be produced in regions of the solar nebula where the water vapor could have been enhanced either by a giant planet "sub-nebula" (Prinn and Fegley, 1987) or by "chondrule-forming" shock waves (Ciesla et al., 2003). This latter model was used to invoke the possible formation of phyllosilicates in FGRs in the solar nebula before the accretion of chondrules into planetesimals (Ciesla et al., 2003). Assuming that chondrules formed by shock waves in the solar nebula (e.g., Connolly and Love, 1998), Ciesla et al. (2003) proposed that the formation of phyllosilicates in FGRs of CM chondrites was the result of a shock wave associated with the chondrule formation, which propagated to a water–ice-rich region of the solar nebula beyond the snow line. The propagation of the shock front through this region would have induced the vaporization of ice particles and raised the water vapor pressure in this region, allowing the production of phyllosilicates. In addition to the model of formation of hydrous phases in the solar nebula, Bischoff (1998) also described another pre-accretionary aqueous alteration model involving the aqueous alteration of anhydrous silicates in relatively small and uncompacted precursor planetesimals, composed of a loosely conglomeration of large inclusion (e.g., chondrules, CAIs), ice and fine-grained material. In this model, melting of accreted ice particles was induced by ^{26}Al-related heating. After the subsequent complete destruction of these precursor bodies, some of the aqueously altered material could have accreted onto chondrules to form the FGRs. While we cannot favor either of these two models based on our data, they suggest that the fine-grained material in FGRs from both CO and CR chondrites could have been affected by similar pre-accretionary aqueous alteration processes in the solar nebula before incorporation into their parent bodies. The type 3 CO and CR chondrites were not affected by significant additional secondary processing on their parent body asteroids and, thus, exhibit higher presolar silicate abundances in the interstitial matrix than in the FGRs, while the type 2 CR chondrites experienced additional aqueous alteration on their parent body, decreasing the presolar silicate abundances in their matrices to values similar to the abundances in the FGRs.

In summary, comparison of the presolar silicate abundances in CO3.0 and CR2-3 chondrites is consistent with a formation of FGRs by accretion of dust grains onto freely-floating chondrules in the solar nebula before their aggregation into their parent body asteroids. The low presolar silicate abundances observed in FGRs of type 3 and type 2 CO and CR chondrites reflect the pre-accretionary aqueous alteration of the fine-grained material in the FGRs by melted water ice associated with either chondrule-forming shock waves in the solar nebula, or ^{26}Al-related heating inside precursor planetesimals.

4.5. Identification of a unique composite FGR (FGR2) in ALHA77307

The observation of this composite FGR in ALHA77307 (Fig. 6) further argues against formation of the FGRs by impact-related compression on the meteorite parent body because compression of matrix material on the parent body asteroid should compress fine-grained material (and the small chondrule) into the larger chondrule. Another interesting characteristic of this composite FGR is that the presolar O-anomalous grain abundances of FGR 2 are much higher than the abundances in the other FGRs in the CO3 chondrites and are, in fact, similar to abundances in the matrix areas of ALHA77307, with O-anomalous and C-anomalous grain abundances of 245 ± 49 ppm and 36^{+24}_{-15} ppm (Figs. 12 and 13), respectively. The higher abundance of presolar silicate grains in FGR 2 appears to reflect its formation from fine-grained material that did not experience the aqueous alteration experienced by most FGRs. As shown in Fig. 6, we propose a model of formation of the composite FGR where dust first accreted around the freely floating small chondrule (FGR 3) in the solar nebula, followed by accretion of the small rimmed chondrule and dust around the large chondrule to form the composite rim (FGR 2). While we do not have any clear constraints on the time between the formation of the rims around the small and large chondrules, the identification of microchondrules in some FGRs of ordinary and carbonaceous chondrites demonstrates that chondrule and FGR formation were contemporary events (e.g., Krot and Rubin, 1996). Based on our data, we cannot definitively exclude a two-stage scenario with the formation of FGR 3 in the solar nebula, followed by formation of the larger chondrule rim by impact-related compression on the asteroid parent body.

However, the absence of deformation of the rim around the small chondrule and the lack of any porosity difference between FGRs 2 and 3 (Fig. 5) makes this scenario rather unlikely.

The observation of a composite FGR thus argues against the impact-related model, but is consistent with the formation of FGRs in the solar nebula before the accretion of chondrules into planetesimals.

4.6. Implications for the models of FGR formation in CO3 chondrites: evidence for nebular origin

The ubiquitous presence of presolar silicate grains in FGRs combined with the similar porosity between interstitial matrix regions and FGRs in LAP 031117 and ALHA77307 (Fig. 5), as well as the identification of a composite FGR (a small rimmed chondrule within a larger chondrule rim; Fig. 6) in ALHA77307 are all consistent with a formation of FGRs by dust accretion onto freely floating chondrules in the solar nebula before their agglomeration in asteroids. This model, however, does not preclude formation of FGRs from different groups of carbonaceous chondrites by different processes and that multiple pre-accretionary and/or asteroidal processes might account for the formation of FGRs.

A recurrent critique of the models of FGR formation in the solar nebula has been the absence of any efficient dust compaction process (e.g., Trigo-Rodriguez et al., 2006; Wasson and Rubin, 2014). However, recent laboratory experiments (Beitz et al., 2013a,b) provide evidence supporting that rims can form in the solar nebula. Furthermore, Ormel et al. (2008) suggested co-accretion of chondrules and dust in the solar nebula prior to parent body formation. In their model, dust accreted onto freely floating chondrules as they move through the dusty nebula gas, and then collisions between rimmed chondrules resulted in the compaction of the FGRs. This model is consistent with recent high-resolution electron backscatter diffraction (EBSD) data in several FGRs in the CV3 chondrite Allende which indicate that chondrule rims in this meteorite have fabrics consistent with a formation in a nebular setting, rather than an asteroidal setting (Bland et al., 2011).

5. CONCLUSIONS AND SUMMARY

Here we report the first self-consistent data set of presolar grain abundances for individual matrix regions and fine-grained chondrule rims (FGRs) in three CO3.0 chondrites (LAP 031111, ALHA77307 and DOM 08006) and use these data to discuss possible models of fine-grained rim formation. All three meteorites are characterized by high overall presolar silicate abundances (~150 ppm), providing further evidence that they are very pristine meteorites that experienced limited thermal or aqueous alteration.

The presence of presolar silicate grains in all FGRs combined with the identification of a composite FGR (a small rimmed chondrule within a larger chondrule rim) in ALHA77307, and the observation of similar porosity between interstitial matrix regions and FGRs in LAP 031117 and ALHA77307 all support a formation of FGRs by dust accretion onto freely floating chondrules in the solar nebula before their incorporation into their parent-body asteroid.

We observed systematically lower abundances of O-anomalous grains in the FGRs than in the matrix areas of LAP 031117, ALHA77307 and DOM 08006 (overall abundances of 186 ± 13 ppm and 67 ± 10 ppm, for the matrix and FGRs respectively), while the C-anomalous grain abundances are similar in all areas (~30 ppm). In LAP 031117, we found a correlation between the lower O-anomalous grain abundances in the FGRs and the mineralogies of these areas. Matrix areas have higher O-anomalous grain abundances and present few signs of aqueous alteration, while a FGR shows clear evidence of extensive aqueous alteration and has significantly lower O-anomalous grain abundances, suggesting the destruction or re-equilibration of the oxygen isotopic compositions of some presolar silicates in the rims by localized (micrometer-scale) aqueous alteration.

Comparison of the O-anomalous and C-anomalous grain abundances in the matrix and individual FGRs of CR2-3 and CO3 chondrites is consistent with the pre-accretionary aqueous alteration of the fine-grained material in the FGRs by melted water ice associated with either chondrule-forming shock waves in the solar nebula, or ^{26}Al-related heating inside precursor planetesimals.

Our coordinated study of the presolar grains abundances, elemental compositions and mineralogy of fine-grained material in the three CO3.0 chondrites provides strong evidence that the fine-grained rims around chondrules in CO3 chondrites formed by dust accretion onto freely floating chondrules in the solar nebula, before incorporation in the meteorite parent body. Our study also confirms that presolar silicates constitute useful tracers of nebular and parent-body processing of fine-grained materials in primitive early solar system materials.

ACKNOWLEDGEMENTS

This study was funded by the NASA Earth and Space Science Fellowship NNX12AN77H (P.H.) and NASA Grants NNX14AG25G (C.F.), NNX12AK47G (T.Z.) and NNX13AM22G (A.W.). We thank the JSC curators and the Meteorite Working Group for the loan of the three meteorite thin sections. We are also grateful to Tim Smolar for maintenance of the NanoSIMS 50 and Auger Nanoprobe at Washington University in St. Louis. We thank Christian Vollmer and an anonymous referee for constructive reviews, as well as comments from associate editor Peter Hoppe, which improved this paper. This work is dedicated to Dr. Ernst Zinner, a pioneer in presolar grain research and secondary-ion mass spectrometry (SIMS).

APPENDIX A. SUPPLEMENTARY MATERIAL

Supplementary data associated with this article can be found, in the online version, at http://dx.doi.org/10.1016/j.gca.2017.06.004.

REFERENCES

Allen J. S., Nozette S. and Wilkening L. (1980) A study of chondrule rims and chondrule irradiation records in unequilibrated ordinary chondrites. *Geochim. Cosmochim. Acta* **44**, 1161–1175.

Alexander C. M. O'. D. (2005) Re-examining the role of chondrules in producing the elemental fractionations in chondrites. *Meteorit. Planet. Sci.* **40**, 943–965.

Amari S., Anders E., Virag A. and Zinner E. (1990) Interstellar graphite in meteorites. *Nature* **345**, 238–240.

Beitz E., Blum J., Mathieu R., Pack A. and Hezel D. C. (2013a) Experimental investigation of the nebular formation of chondrule rims and the formation of chondrite parent bodies. *Geochim. Cosmochim. Acta* **116**, 41–51.

Beitz E., Guettler C., Nakamura A. M., Tsuchiyama A. and Blum J. (2013b) Experiments on the consolidation of chondrites and the formation of dense rims around chondrules. *Icarus* **225**, 558–569.

Bernatowicz T., Fraundorf G., Tang M., Anders E., Wopenka B., Zinner E. and Fraundorf P. (1987) Evidence for interstellar SiC in the Murray carbonaceous meteorite. *Nature* **330**, 728–730.

Bigolski J. N., Frank D. R., Zolensky M. E., Weisberg M. K., Ebel D. S. and Rahman Z. (2013) A Microanalytical (TEM) study of fine-grained chondrule rims in NWA 5717. In: 76th Annual Meteoritical Society Meeting, #5227 (abstr.).

Bischoff A. (1998) Aqueous alteration of carbonaceous chondrites: evidence for preaccretionary alteration – a review. *Meteorit. Planet. Sci.* **33**, 1113–1122.

Bland P. A., Collins G. S., Davison T. M., Abreu N. M., Ciesla F. J., Muxworthy A. R. and Moore J. (2014) Pressure-temperature evolution of primordial Solar System solids during impact-induced compaction. *Nat. Commun.* **5**, 5451.

Bland P. A., Howard L. E., Prior D. J., Wheeler J., Hough R. M. and Dyl K. A. (2011) Earliest rock fabric formed in the Solar System preserved in a chondrule rim. *Nat. Geosci.* **4**, 244–247.

Bland P. A., Muxworthy A. R., Collins G. S., Moore J., Davison T. M., Prior D. J., Wheeler J., Ciesla F. J. and Dyl K. A. (2012) Effect of low intensity impacts on chondrite matrix, Lunar Planet. Sci. XLIII, #2005 (abstr.).

Bonal L., Bourot-Denise M., Quirico E., Montagnac G. and Lewin E. (2007) Organic matter and metamorphic history of CO chondrites. *Geochim. Cosmochim. Acta* **71**, 1605–1623.

Bonal L., Quirico E., Bourot-Denise M. and Montagnac G. (2006) Determination of the petrologic type of CV3 chondrites by Raman spectroscopy of included organic matter. *Geochim. Cosmochim. Acta* **70**, 1849–1863.

Bonal L., Quirico E., Flandinet L. and Montagnac G. (2016) Thermal history of type 3 chondrites from the Antarctic meteorite collection determined by Raman spectroscopy of their polyaromatic carbonaceous matter. *Geochim. Cosmochim. Acta* **189**, 312–337.

Bose M., Floss C. and Stadermann F. J. (2010a) An investigation into the origin of Fe-rich presolar silicates in Acfer 094. *Astrophys. J.* **714**, 1624–1636.

Bose M., Floss C., Stadermann F. J., Stroud R. M. and Speck A. K. (2012) Circumstellar and interstellar material in the CO3 chondrite ALHA77307: an isotopic and elemental investigation. *Geochim. Cosmochim. Acta* **93**, 77–101.

Bose M., Zhao X., Floss C., Stadermann F. J. and Lin Y. (2010b) Stardust material in the paired enstatite chondrites: SAH 97096 and SAH 97159. Proceeding of Science (NIC-XI), 138.

Brearley A. J. (1993) Matrix and fine-grained rims in the unequilibrated CO3 chondrite, ALHA77307 - Origins and evidence for diverse, primitive nebular dust components. *Geochim. Cosmochim. Acta* **57**, 1521–1550.

Buseck P. R. and Hua X. (1993) Matrices of carbonaceous chondrite meteorites. *Ann. Rev. Earth Planet. Sci.* **21**, 255–305.

Chizmadia L. J. and Cabret-Lebron E. (2009) LaPaz 031117: a new primitive CO3 carbonaceous chondrite, Lunar Planet. Sci. XL, #2031 (abstr.).

Chizmadia L. J., Rubin A. E. and Wasson J. T. (2002) Mineralogy and petrology of amoeboid olivine inclusions in CO3 chondrites: Relationship to parent body aqueous alteration. *Meteorit. Planet. Sci.* **38**, 1781–1796.

Choi B.-G., Huss G. R., Wasserburg G. J. and Gallino R. (1998) Presolar corundum and spinel in ordinary chondrites: origins from AGB stars and a supernova. *Science* **282**, 1284–1289.

Ciesla F. J., Lauretta D. S., Cohen B. A. and Hood L. L. (2003) A nebular origin for chondritic fine-grained phyllosilicates. *Science* **299**, 549–552.

Connolly H. C. and Love S. G. (1998) The formation of chondrules: petrologic tests of the shock wave model. *Science* **280**, 62–67.

Consolmagno G. J., Britt D. T. and Macke R. J. (2008) The significance of meteorite density and porosity. *Chem. Der Erde-Geochem.* **68**, 1–29.

Croat T. K., Haenecour P. and Floss C. (2015) FIB-TEM studies of a presolar SiC and the surrounding matrix in a primitive CO3.0 chondrite. Lunar Planet. Sci. XLVI, #2135 (abstr.).

Cuzzi J. N. (2004) Blowing in the wind: III. Accretion of dust rims by chondrule-sized particles in a turbulent protoplanetary nebula. *Icarus* **168**, 484–497.

Davidson J., Busemann H. and Franchi I. A. (2012) Presolar grain inventory of a fine-grained chondrule rim in CO3.0 chondrite ALHA 77307. Meteorit. Planet. Sci. Suppl. #5269 (abstr.).

Davidson J., Busemann H., Nittler L. R., Alexander C. M. O'D., Orthous-Daunay F.-R., Franchi I. A. and Hoppe P. (2014a) Abundances of presolar silicon carbide grains in primitive meteorites determined by NanoSIMS. *Geochim. Cosmochim. Acta* **139**, 248–266.

Davidson J., Nittler L. R., Alexander C. M. O'D. and Stroud R. M. (2014b) Petrography of very primitive CO3 chondrites: Dominion Range 08006, Miller Range 07687, and four others. Lunar Planet. Sci. XLV, #1384 (abstr.).

Dyl K. A., Bland P. A., Muxworthy A. R., Collins G. S., Davison T. M., Prior D. J. and Ciesla, F. J. (2012) Compositional effects of low-pressure impacts in chondritic meteorites: oxygen isotope homogenization and Mg-Fe diffusion in matrix olivine and presolar grains. Lunar Planet. Sci. XLIII, #2251 (abstr.).

Fegley B. and Prinn R. G. (1989) Solar nebula chemistry - Implications for volatiles in the Solar System. In *The Formation and Evolution of Planetary Systems* (eds. H. A. Weaver and L. Danly), pp. 171–205.

Floss C. and Brearley A. J. (2014) Presolar grain abundance variations in the unique carbonaceous chondrite MIL 07687. Meteorit. Planet. Sci 49, #5183 (abstr.).

Floss C. and Haenecour P. (2016a) Presolar silicate grains: abundances, isotopic and elemental compositions, and the effects of secondary processing. *Geochem. J.* **50**, 3–25.

Floss C. and Haenecour P. (2016b) Meteorite Hills (MET) 00526: An unequilibrated ordinary chondrite with high presolar grain abundances. Lunar Planet. Sci. XLVII, #1030 (abstr.).

Floss C. and Stadermann F. (2009a) Auger nanoprobe analysis of presolar ferromagnesian silicate grains from primitive CR chondrites QUE 99177 and MET 00426. *Geochim. Cosmochim. Acta* **73**, 2415–2440.

Floss C. and Stadermann F. (2009b) High abundances of circumstellar and interstellar C-anomalous phases in the primitive CR3 chondrites QUE 99177 and MET 00426. *Astrophys. J.* **697**, 1242–1255.

Floss C. and Stadermann F. J. (2012) Presolar silicate and oxide abundances and compositions in the ungrouped carbonaceous chondrite Adelaide and the K chondrite Kakangari: The effects of secondary processing. *Meteorit. Planet. Sci.* **47**, 992–1009.

Floss C., Stadermann F. J. and Bose M. (2008) Circumstellar Fe oxide from the Acfer 094 carbonaceous chondrite. *Astrophys. J.* **672**, 1266–1271.

Gehrels N. (1986) Confidence limits for small numbers of events in astrophysical data. *Astrophys. J.* **303**, 336–346.

Greenwood R. C. and Franchi I. A. (2004) Alteration and metamorphism of CO3 chondrites: evidence from oxygen and carbon isotopes. *Meteorit. Planet. Sci* **39**(11), 1823–1838.

Greshake A., Krot A. N., Flynn G. J. and Keil K. (2005) Fine-grained dust rims in the Tagish Lake carbonaceous chondrite: evidence for parent body alteration. *Meteorit. Planet. Sci* **40**(9/10), 1413–1431.

Grossman J. N. and Brearley A. J. (2005) The onset of metamorphism in ordinary and carbonaceous chondrites. *Meteorit. Planet. Sci.* **40**, 87–122.

Gyngard F., Nittler L. R., Zinner E., Jose J. and Cristallo S. (2011) New reaction rates and implications for nova nucleosynthesis and presolar grains. Lunar Planet. Sci. XLII, #2675.

Haenecour P. and Floss C. (2011) High Abundance of stardust in the CO3.0 chondrite LaPaz 031117. Meteorit. Planet. Sci 74, #5009 (abstr.).

Haenecour P. and Floss C. (2012) Stardust in fine-grained chondrule rims and matrix in LaPaz 031117: insights into the conditions of dust accretion in the solar nebula. Lunar Planet. Sci. XLIII, #1107 (abstr.).

Haenecour P. and Floss C. (2016) Stardust in the CO3.0 chondrite NWA 8631: low abundance of presolar silicates. Meteorit. Planet. Sci 51, #6209 (abstr.).

Haenecour P., Floss C., Jolliff B. L. and Carpenter P. (2013a) Presolar grains in fine-grained chondrule rims: re-equilibration of oxygen isotopic compositions in some presolar silicates by heating. Lunar Planet. Sci. XLIV, #1150 (abstr.).

Haenecour P., Floss C., Jolliff B. L., Zega T. J., Bose M. and Carpenter P. (2014) Presolar silicates as tracers of the formation of fine-grained chondrule rims in CO3 chondrites. Lunar Planet. Sci. XLV, #1316. (abstr.).

Haenecour P., Floss C., José J., Amari S., Lodders K., Jadhav M., Wang A. and Gyngard F. (2016a) Coordinated analysis of two graphite grains from the CO3.0 LAP 031117 meteorite: first identification of a CO nova graphite and a presolar iron sulfide subgrain. *Astrophys. J.* **825**, 88.

Haenecour P., Floss C. and Yada T. (2012) Heterogeneous distribution of supernova silicate and oxide grains in the Solar System? Meteorit. Planet. Sci 75, #5220 (abstr.).

Haenecour P., Floss C., Zega T. J., Croat T. K. Jolliff B. L. and Carpenter P. (2017). Pre-accretionary aqueous alteration of dust in fine-grained chondrule rims: evidence from presolar grain abundances and mineralogy in primitive CO3.0 chondrites. Lunar Planet. Sci. XLVIII, #2222 (abstr.).

Haenecour P., Floss C., Zega T. J. and Ogliore R. (2016b) Auger spectroscopy analysis of submicron-sized silicate grains in Chondrites: Insight into their aqueous and thermal alteration history. Meteorit. Planet. Sci 51, #6354 (abstr.).

Haenecour P., Zega T. J., Floss C., Croat T. K. and Jolliff B. L. (2015) Abundances and elemental compositions of presolar silicates in CO3.0 chondrites: possible indicators of secondary processing? Lunar Planet. Sci. XLVI, #1160 (abstr.).

Haenecour P., Zhao X., Floss C., Lin Y. and Zinner E. (2013b) First laboratory observation of silica grains from core collapse supernovae. *Astrophys. J. Lett.* **768**.

Huss G. R., Hutcheon I. D. and Wasserburg G. J. (1997) Isotopic systematics of presolar silicon carbide from the orgueil (CI) chondrite: implications for Solar System formation and stellar nucleosynthesis. *Geochim. Cosmochim. Acta* **61**, 5117–5148.

Huss G. R. and Lewis R. S. (1994) Noble-Gases in presolar diamonds.2. component abundances reflect thermal-processing. *Meteoritics* **29**, 811–829.

Huss G. R. and Lewis R. S. (1995) Presolar diamond, SiC, and graphite in primitive chondrites - abundances as a function of meteorite class and petrologic type. *Geochim. Cosmochim. Acta* **59**, 115–160.

Huss G. R., Lewis R. S. and Hemkin S. (1996) The "normal planetary" noble gas component in primitive chondrites: compositions, carrier, and metamorphic history. *Geochim. Cosmochim. Acta* **60**, 3311–3340.

Huss G. R., Meshik A. P., Smith J. B. and Hohenberg C. M. (2003) Presolar diamond, silicon carbide, and graphite in carbonaceous chondrites: implications for thermal processing in the solar nebula. *Geochim. Cosmochim. Acta* **67**, 4823–4848.

Huss G. R., Rubin A. E. and Grossman J. N. (2006) Thermal Metamorphism in Chondrites. In *Meteorites and the Early Solar System II* (eds. D. S. Lauretta and , Jr.H. Y. McSween). University of Arizona Press, Tucson, 943 pp., pp. 567–586.

Hynes K. M. and Gyngard F. (2009) The presolar grain database: http://presolar.wustl.edu/~pgd. Lunar Planet. Sci. XL, #1198 (abstr.).

Jarosewich E. (1990) Chemical analyses of meteorites - A compilation of stony and iron meteorite analyses. *Meteoritics* **25**, 323–337.

Keller L. P. and Messenger S. (2011) On the origins of GEMS grains. *Geochim. Cosmochim. Acta* **75**, 5336–5365.

King T. V. V. and King E. A. (1981) Accretionary dark rims in unequilibrated chondrites. *Icarus* **48**(3), 460–472.

Krot A. N., Keil K., Scott E. R. D., Goodrich C. A. and Weisberg M. K. (2014) 1.1 - Classification of meteorites and their genetic relationships. In *Treatise on Geochemistry (Second Edition)* (ed. H. D. H. K. Turekian). Elsevier, Oxford, pp. 1–63.

Krot A. N. and Rubin A. E. (1996) Microchondrule-bearing chondrule rims: constraints on chondrule formation. In *Chondrules and the Protoplanetary Disk* (eds. R. H. Hewins, R. H. Jones and E. R. D. Scott). Cambridge University Press, pp. 181–184.

Lauretta D. S., Hua X. and Buseck P. R. (2000) Mineralogy of fine-grained rims in the alh 81002 cm chondrite. *Geochim. Cosmochim. Acta* **64**(19), 3263–3273.

Le Guillou C. and Brearley A. (2014) Relationships between organics, water and early stages of aqueous alteration in the pristine CR3.0 chondrite MET 00426. *Geochim. Cosmochim. Acta* **131**, 344–367.

Leitner J., Hoppe P. and Zipfel J. (2015) Distribution and abundance of presolar silicate and oxide stardust in CR chondrites. Lunar Planet. Sci. XLVI, #1874 (abstr.).

Leitner J., Hoppe P. and Zipfel J. (2016a) The presolar grain inventory of the CR chondrite Elephant Moraine 92161. Lunar Planet. Sci. XLVII, #1873 (abstr.).

Leitner J., Metzler K. and Hoppe P. (2014) Characterization of presolar grains in cluster chondrite clasts from unequilibrated ordinary chondrites. Lunar Planet. Sci. XLV, #1099 (abstr.).

Leitner J., Vollmer C., Floss C., Zipfel J. and Hoppe P. (2016b) Ancient stardust in fine-grained chondrule dust rims from carbonaceous chondrites. *Earth Planet. Sci. Lett.* **434**, 117–128.

Leitner J., Vollmer C., Hoppe P. and Zipfel J. (2012) Characterization of presolar material in the CR chondrite Northwest Africa 852. *Astrophys. J.* **745** (16pp) 38.

Lewis R. S., Ming T., Wacker J. F., Anders E. and Steel E. (1987) Interstellar diamonds in meteorites. *Nature* **326**, 160–162.

Lugaro M., Karakas A. I., Bruno C. G., Aliotta M., Nittler L. R., Bemmerer D., Best A., Boeltzig A., Broggini C., Caciolli A., Cavanna F., Ciani G. F., Corvisiero P., Davinson T., Depalo R., Di Leva A., Elekes Z., Ferraro F., Formicola A., Fülop Zs., Gervino G., Guglielmetti A., Gustavino C., Gyürky Gy., Imbriani G., Junker M., Menegazzo R., Mossa V., Pantaleo F. R., Piatti D., Prati P., Scott D. A., Straniero O., Strieder F., Szücs T., Takács M. P. and Trezzi D. (2017) Origin of meteoritic stardust unveiled by a revised proton-capture rate of ^{17}O. *Nature Astronomy* **1**(0027), 1–5.

McSween H. Y. (1977) Carbonaceous chondrites of Ornans-type - metamorphic sequence. *Geochim. Cosmochim. Acta* **41**, 477.

McSween, Jr., H. Y. and Huss G. R. (2010) *Cosmochemistry*. Cambridge University Press.

Messenger S., Keller L. P. and Lauretta D. S. (2005) Supernova olivine from cometary dust. *Science* **309**, 737–741.

Messenger S., Keller L. P., Stadermann F. J., Walker R. M. and Zinner E. (2003) Samples of stars beyond the Solar System: silicate grains in interplanetary dust. *Science* **300**, 105–108.

Metzler K. (2004) Formation of accretionary dust mantles in the solar nebula: evidence from preirradiated olivines in CM chondrites. *Meteorit. Planet. Sci.* **39**, 1307–1319.

Metzler K., Bischoff A. and Stöffler D. (1992) Accretionary dust mantles in CM chondrites: evidence for solar nebula processes. *Geochim. Cosmochim. Acta* **56**, 2873–2897.

Morfill G. E., Durisen R. H. and Turner G. W. (1998) An accretion rim constraint on chondrule formation theories. *Icarus* **134**, 180–184.

Nguyen A. N., Nittler L. R., Stadermann F. J., Stroud R. M. and Alexander C. M. O'. D. (2010) Coordinated analyses of presolar grains in the Allan Hills 77307 and Queen Elizabeth Range 99177 meteorites. *Astrophys. J.* **719**, 166–189.

Nguyen A. N., Stadermann F. J., Zinner E., Stroud R. M., Alexander C. M. O'. D. and Nittler L. R. (2007) Characterization of presolar silicate and oxide grains in primitive carbonaceous chondrites. *Astrophys. J.* **656**, 1223–1240.

Nguyen A. N. and Zinner E. (2004) Discovery of ancient silicate stardust in a meteorite. *Science* **303**, 1496–1499.

Nittler L. R. (2009) Presolar Stardust in the Solar System: Recent Advances for Nuclear Astrophysics. In: proceedings of the 10th Symposium on Nuclei in the Cosmos, PoS(NIC X) 013.

Nittler L. R., Alexander C. M. O'. D., Gallino R., Hoppe P., Nguyen A. N., Stadermann F. J. and Zinner E. (2008) Aluminum-, calcium- and titanium-rich oxide stardust in ordinary chondrite meteorites. *Astrophys. J.* **682**, 1450–1478.

Nittler L. R., Alexander C. M. O'D., Gao X., Walker R. M. and Zinner E. (1997) Stellar sapphires: the properties and origins of presolar Al_2O_3 in meteorites. *Astrophys. J.* **483**, 475–495.

Nittler L. R., Alexander C. M. O'D. and Stroud R. M. (2013) High abundance of presolar materials in CO3 chondrite Dominion Range 08006, Lunar Planet. Sci. XLIV, #2367 (abstr.).

Nollett K. M., Busso M. and Wasserburg G. J. (2003) Cool bottom processes on the thermally pulsing asymptotic giant branch and the isotopic composition of circumstellar dust grains. *Astrophys. J.* **582**, 1036–1058.

Ormel C. W., Cuzzi J. N. and Tielens A. G. G. M. (2008) Co-accretion of chondrules and dust in the solar nebula. *Astrophys. J.* **679**, 1588–1610.

Prinn R. G. and Fegley B. (1987) The atmospheres of Venus, Earth, and Mars - a critical comparison. *Annu. Rev. Earth Planet. Sci.* **15**, 171–212.

Scott E. R. D. and Jones R. H. (1990) Disentangling nebular and asteroidal features of CO3 carbonaceous chrondrite meteorites. *Geochim. Cosmochim. Acta* **54**, 2485–2502.

Scott E. R. D. and Krot A. N. (2014) 1.2 - Chondrites and Their Components. In *Treatise on Geochemistry (Second Edition)* (ed. H. D. H. K. Turekian). Elsevier, Oxford, pp. 65–137.

Sears D. W. G. (2011) *The origin of chondrules and chondrites*. Cambridge University Press.

Sears D. W. G., Batchelor J. D., Lu J. and Keck B. D. (1991) Metamorphism of CO and CO-like chondrites and comparisons with type 3 ordinary chondrites. *Proc. NIPR Sympos. Antarctic Meteorites* **4**, 319–343.

Sears D. W. G., Benoit P. H. and Lu J. (1993) Two chondrule groups each with distinctive rims in Murchison recognized by cathodoluminescence. *Meteoritics* **28**, 669–675.

Seddio S. M., Jolliff B. L., Korotev R. L. and Carpenter P. K. (2014) Thorite in an Apollo 12 granite fragment and age determination using the electron microprobe. *Geochim. Cosmochim. Acta* **135**, 307–320.

Simon S. B. and Grossman L. (2015) Refractory inclusions in the pristine carbonaceous chondrites DOM 08004 and DOM 08006. *Meteorit. Planet. Sci.* **50**, 1032–1049.

Stadermann F. J., Floss C., Bose M. and Lea A. S. (2009) The use of Auger spectroscopy for the in situ elemental characterization of sub-micrometer presolar grains. *Meteorit. Planet. Sci.* **44**, 1033–1049.

Takayama A. and Tomeoka K. (2012) Fine-grained rims surrounding chondrules in the Tagish Lake carbonaceous chondrite: verification of their formation through parent-body processes. *Geochim. Cosmochim. Acta* **98**, 1–18.

Tomeoka K. and Tanimura I. (2000) Phyllosilicate-rich chondrule rims in the vigarano cv3 chondrite: evidence for parent-body processes. *Geochim. Cosmochim. Acta* **64**, 1971–1988.

Trigo-Rodriguez J. M., Rubin A. E. and Wasson J. T. (2006) Non-nebular origin of dark mantles around chondrules and inclusions in CM chondrites. *Geochim. Cosmochim. Acta* **70**, 1271–1290.

Vogel N., Wieler R., Bischoff A. and Baur H. (2003) Microdistribution of primordial Ne and Ar in fine-grained rims, matrices, and dark inclusions of unequilibrated chondrites—Clues on nebular processes. *Meteorit. Planet. Sci* **38**(9), 1399–1418.

Vollmer C., Hoppe P., Stadermann F. J., Floss C. and Brenker F. E. (2009) NanoSIMS analysis and Auger electron spectroscopy of silicate and oxide stardust from the carbonaceous chondrite Acfer 094. *Geochim. Cosmochim. Acta* **73**, 7127–7149.

Wasserburg G. J., Boothroyd A. I. and Sackmann I.-J. (1995) Deep circulation in red giant stars: a solution to the carbon and oxygen isotope puzzles? *Astrophys. J.* **447**, L37–L40.

Wilkening L. L. and Hill D. H. (1985) Fine-Grained Chondrule Rims. Meteoritics, Vol. 20, p. 785 (abstr.).

Wasson J. T. and Rubin A. E. (2014) Absence of matrix-like chondrule rims in CR2 LAP 02342. *Meteorit. Planet. Sci.* **49**(2), 245–260.

Yada T., Floss C., Stadermann F. J., Zinner E., Nakamura T., Noguchi T. and Lea A. S. (2008) Stardust in Antarctic micrometeorites. *Meteorit. Planet. Sci.* **43**, 1287–1298.

Zega T. J. and Buseck P. R. (2003) Fine-grained-rim mineralogy of the Cold Bokkeveld CM chondrite. *Geochim. Cosmochim. Acta* **67**, 1711–1721.

Zega T. J., Haenecour P., Floss C. and Howe J. Y. (2017) Polycrystalline presolar spinel identified in the DOM 08006 CO3.0 chondrite. 80th Annual Meeting of the Meteoritical Society, abstract #6319 (abstr.).

Zega T. J., Haenecour P., Floss C. and Stroud R. M. (2015) Circumstellar magnetite from the LAP 031117 CO3.0 chondrite. *Astrophys. J.* **808**, 55.

Zega T. J., Haenecour P., Floss C., and Stroud R. M. (2014) Extraction and analysis of presolar grains from the LAP 031117 CO3.0 chondrite. Lunar Planet. Sci. XLV, #2256 (abstr.).

Zega T. J., Nittler L. R., Busemann H., Hoppe P. and Stroud R. M. (2007) Coordinated isotopic and mineralogic analyses of planetary materials enabled by in situ lift-out with a focused ion beam scanning electron microscope. *Meteorit. Planet. Sci.* **42**, 1373–1386.

Zhao X., Floss C., Lin Y. and Bose M. (2013) Stardust investigation into the CR chondrite Grove Mountain 021710. *Astrophys. J.* **769** (16pp) 49.

Zhao X., Floss C., Stadermann F. J., Bose M. and Lin, Y. (2011) Continued investigation of presolar silicate grains in the carbonaceous chondrite Ningqiang. Lunar Planet. Sci. XLII, #1982. (abstr.).

Zhao X., Stadermann F. J., Floss C., Bose M. and Lin Y. (2010) Characterization of presolar grains from the carbonaceous chrondrite Ningqiang. Lunar Planet. Sci. XLI, #1431. (abstr.).

Zinner E. (2014) 1.4 - Presolar Grains. In *Treatise on Geochemistry (Second Edition)* (ed. H. D. H. K. Turekian). Elsevier, Oxford, pp. 181–213.

Associate editor: Peter Hoppe